

## $\mu$ -Atomic Hyperfine Structure in the $K$ , $L$ , and $M$ Lines of $U^{238}$ and $Th^{232}$ \* †

R. J. McKEE ‡

*Department of Physics and the Enrico Fermi Institute for Nuclear Studies,  
University of Chicago, Chicago, Illinois 60637*

(Received 27 May 1968; revised manuscript received 25 November 1968)

The  $\mu$ -atomic hyperfine structure in the  $K$ ,  $L$ , and  $M$  lines of  $U^{238}$  and  $Th^{232}$  was obtained using a large high-resolution Ge(Li) detector. The hyperfine structure is due to large deformations in these nuclei and arises from a dynamic electric quadrupole interaction between the muonic states and the lowest nuclear states. The measurements were interpreted using the Bohr-Mottelson rigid-rotator model with a symmetry axis for the nucleus and taking into account the first and second rotational states. The charge distribution chosen was a Fermi type whose constant-density shells are concentric ellipsoids of revolution of constant eccentricity. By numerically solving the Dirac equation, it was possible to determine three parameters of the size and shape of the nuclear charge distribution. The intrinsic quadrupole moments were found to be  $(11.47 \pm 0.13) \times 10^{-24}$  and  $(9.83 \pm 0.16) \times 10^{-24}$  cm<sup>2</sup> for  $U^{238}$  and  $Th^{232}$ , respectively, in good agreement with other measurements. The deformation parameter  $\beta$  was found to be  $0.244 \pm 0.002$  and  $0.222 \pm 0.003$ , respectively. The central density, found to be  $0.153 \pm 0.002$  and  $0.153 \pm 0.003$  nucleons per cubic fermi, respectively, differs only slightly from the value of 0.158 nucleons per cubic fermi that one finds for most spherical nuclei.

### I. INTRODUCTION

THE usefulness of the muon as a nuclear probe was first recognized by Wheeler,<sup>1,2</sup> whose original papers still serve as the basic guide to the subject. Wheeler pointed out that from measurements of muonic x rays the shape as well as the extent of the nuclear charge distribution could be determined. This method for determining nuclear charge radii has been used extensively following the pioneer experiments of Fitch and Rainwater.<sup>3</sup> It complements the determination of the same quantity from electron scattering measurements.<sup>4</sup>

Among the effects considered by Wheeler in his 1953 paper<sup>2</sup> was the hyperfine splitting induced by the static electric quadrupole moment of the nucleus. This is entirely analogous to that produced by an electron but much larger because the muon moves much closer to the nucleus. Such effects occur only for nuclei with nuclear spin  $I \geq 1$  and muon orbits with  $j \geq \frac{3}{2}$ .

Subsequently, Wilets<sup>5</sup> and Jacobsohn<sup>6</sup> reconsidered this problem, giving particular attention to the highly deformed nuclei. Such nuclei have low-lying rotational states which give rise to a novel effect. In the presence of the muon in a low-lying atomic state the low-lying rotational states mix with the ground state by quadrupole interaction. A complex hfs results which appears even when the nuclear spin is zero or  $\frac{1}{2}$ .

The early observations<sup>7-9</sup> made with NaI showed very little of the detail of the line structure which the dynamic quadrupole effect can produce. However, from a careful analysis of the broadened line shapes obtained it was possible to establish the existence of the effect and to use it in a determination of the sign and magnitude of the quadrupole moment.

The development of Ge(Li) detectors<sup>10</sup> made it possible to observe hfs effects with much higher resolution. Such a measurement was first reported by Anderson *et al.*<sup>11</sup> in this laboratory. The present work was carried out as an extension of that initial effort, using a number of refinements of technique in an attempt to reveal the dynamic quadrupole effect in as much detail as possible with the means currently available. The suggestion by Jacobsohn<sup>6</sup> and Wilets<sup>5</sup> that such measurements of muonic x rays could serve to determine the intrinsic quadrupole moments of even-even nuclei is realized in this work for  $Th^{232}$  and  $U^{238}$ . During the course of this work, other reports have appeared<sup>12-14</sup> with which a comparison will be made.

Section II reviews the theory of the muonic atom

\* Submitted in partial fulfillment of the requirements for the Ph.D. degree.

† Research supported by the U.S. National Science Foundation and the National Research Council of Canada.

‡ Present address: National Research Council of Canada, Ottawa, Canada.

<sup>1</sup> J. A. Wheeler, *Rev. Mod. Phys.* **21**, 133 (1949).

<sup>2</sup> J. A. Wheeler, *Phys. Rev.* **92**, 812 (1953).

<sup>3</sup> V. L. Fitch and J. Rainwater, *Phys. Rev.* **92**, 789 (1953).

<sup>4</sup> B. Hahn, D. G. Ravenhall, and R. Hofstadter, *Phys. Rev.* **101**, 1131 (1956); R. Hofstadter, *Ann. Rev. Nucl. Sci.* **7**, 231 (1957).

<sup>5</sup> L. Wilets, *Kgl. Danske Videnskab. Selskab, Mat.-Fys. Medd.* **29**, No. 3 (1954).

<sup>6</sup> B. A. Jacobsohn, *Phys. Rev.* **96**, 1637 (1954).

<sup>7</sup> R. D. Ehrlich, R. J. Powers, V. L. Telegdi, J. A. Bjorkland, S. Raboy, and C. C. Trail, in *Proceedings of the Twelfth Annual Conference on High-Energy Physics, Dubna, 1964* (Atomizdat, Moscow, 1965), Vol. 1, p. 874; *Phys. Rev. Letters* **13**, 550 (1964).

<sup>8</sup> G. Backenstoss, K. Goebel, B. Stadler, U. Hegel, and D. Quitmann, *Nucl. Phys.* **62**, 449 (1965).

<sup>9</sup> H. L. Acker, H. Marschall, G. Backenstoss, and D. Quitmann, *Nucl. Phys.* **62**, 477 (1965).

<sup>10</sup> G. T. Ewan and A. J. Tavendale, *Can. J. Phys.* **42**, 2286 (1964).

<sup>11</sup> H. L. Anderson, C. K. Hargrove, E. P. Hincks, and A. J. Tavendale, in *Proceedings of the Twelfth Annual Conference on High-Energy Physics, Dubna, 1964* (Atomizdat, Moscow, 1965), Vol. 1, p. 936.

<sup>12</sup> H. L. Acker, G. Backenstoss, C. Daum, J. C. Sens, and S. A. De Wit, *Phys. Letters* **14**, 317 (1965).

<sup>13</sup> R. E. Cote, R. Guso, S. Raboy, R. A. Corrigan, Jr., A. Gaigalas, R. B. Sutton, and C. C. Trail, *Phys. Letters* **19**, 18 (1965).

<sup>14</sup> S. A. De Wit, G. Backenstoss, C. Daum, J. C. Sens, and H. L. Acker, *Nucl. Phys.* **87**, 657 (1967).

with a view to establishing the notation used in the hfs formalism and for discussing the Dirac equation which must be solved numerically to relate the energy parameters of the hfs formalism with specific distorted charge distributions. Also included in Sec. II is a discussion of the various corrections that are made to the energy levels calculated from the Dirac equation. Section III outlines the hfs formalism.

The material of Secs. IV and V can be found in greater detail elsewhere.<sup>15</sup> Section IV describes the apparatus used in obtaining the muonic x-ray spectra, and Sec. V describes the data-reduction methods and also includes the Pb<sup>206</sup> muonic x-ray results which were used as the calibration standard for the U<sup>238</sup> and Th<sup>232</sup> spectra.

Section VI describes the fits to the U<sup>238</sup> and Th<sup>232</sup> spectra using the hfs formalism, Sec. VII describes the extraction of the nuclear parameters, including the quadrupole moments, using a specific charge distribution, Sec. VIII compares the present results with other work done on U<sup>238</sup> and Th<sup>232</sup>, Sec. IX is a discussion of the quadrupole moment, and Sec. X concludes the paper.

## II. THEORY

### A. Monopole Interaction

The muonic atom is best described by the relativistic Dirac equation, since the muon in the field of a heavy nucleus has an energy in the lowest states which is an appreciable fraction of the rest mass of the muon. In addition, except for the anomalous part, the Dirac equation has the proper fine-structure splitting built in.

The Hamiltonian of the muon is written

$$H(\mathbf{r}, \boldsymbol{\sigma}) = c\boldsymbol{\alpha} \cdot \mathbf{p} + \beta mc^2 + V(\mathbf{r}), \quad (1)$$

where  $m$  is the muon mass and  $V(\mathbf{r})$  is the electrostatic potential energy of the muon in the field of the nucleus. The quantities  $\boldsymbol{\alpha}$  and  $\beta$  are the usual  $4 \times 4$  Dirac matrices. Only the electrostatic potential of the nucleus is included here; other effects, such as vacuum polarization, are small or negligible and will be dealt with later.

The quantity  $\rho(\mathbf{r})$  stands for the charge distribution of the nucleus and is normalized to  $Z$ , the charge number of the nucleus. With this normalization the monopole term of a multipole expansion of  $V(\mathbf{r})$  in terms of spherical harmonics is

$$\phi(r) = -\frac{Ze^2}{r} + \frac{4\pi e^2}{r} \int_r^\infty \bar{\rho}(r') (r'^2 - rr') dr', \quad (2)$$

where the angular-averaged charge distribution  $\bar{\rho}(r)$  is defined by

$$\bar{\rho}(r) = (4\pi)^{-1} \int \rho(\mathbf{r}) d\Omega. \quad (3)$$

<sup>15</sup>H. L. Anderson, C. K. Hargrove, E. P. Hincks, J. D. McAndrew, R. J. McKee, R. D. Bartonk, and D. Kessler (unpublished).

The monopole term has no angular dependence. For a spherically symmetric nucleus, only the monopole term appears in the expansion.

Using the monopole term, we define a new Hamiltonian:

$$H_0(\mathbf{r}, \boldsymbol{\sigma}) = c\boldsymbol{\alpha} \cdot \mathbf{p} + \beta mc^2 + \phi(r). \quad (4)$$

The Dirac equation that is solved is

$$H_0\psi = E\psi. \quad (5)$$

For low- $Z$  nuclei or for the higher levels of high- $Z$  nuclei, it is sufficient to use the point-nucleus eigenvalues which are available in analytic form.<sup>16</sup> A correction for the effect of finite size of the nucleus may be obtained from a first-order perturbation calculation using the second term in the expression (2). However, for the cases of interest here—the lowest levels in high- $Z$  nuclei—Eq. (5) must be solved by numerical integration.

Equation (5) describes the muon in a central potential field. In this case, the eigenfunctions for muon states  $nlj\mu$ , where  $\mu$  is the  $z$  component of  $j$ , are

$$\begin{aligned} \psi_{n\kappa\mu}(\mathbf{r}) &= (1/r)G_{n\kappa}(r)\chi_{\kappa\mu}(\theta, \phi) \\ &= (i/r)F_{n\kappa}(r)\chi_{-\kappa\mu}(\theta, \phi), \end{aligned} \quad (6)$$

where  $F$  and  $G$ , the small and large components, respectively, are real and have the normalizations

$$\int_0^\infty (F^2 + G^2) dr = 1. \quad (7)$$

The quantum number  $\kappa$  is related to  $l$  and  $j$  by

$$\begin{aligned} j &= |\kappa| - \frac{1}{2}, \\ l &= \kappa, \quad \text{for } \kappa > 0, \\ l &= -(\kappa + 1), \quad \text{for } \kappa < 0. \end{aligned} \quad (8)$$

The radial wave functions satisfy the two coupled differential equations

$$\begin{aligned} F'(r) &= \kappa F(r)/r - [E - mc^2 - \phi(r)]G(r)/\hbar c, \\ G'(r) &= -\kappa G(r)/r + [E + mc^2 - \phi(r)]F(r)/\hbar c. \end{aligned} \quad (9)$$

### B. Radiative Corrections

The eigenvalues that come from a numerical solution of Eq. (9) do not describe the energy levels of the muonic atom accurately enough, even for a spherically symmetric nucleus. Several corrections must be considered.

The most important correction is the electronic vacuum polarization. This effect arises from the emission and reabsorption of virtual electron-positron pairs which cause the vacuum to act like a classical dielectric medium. To order  $\alpha = e^2/\hbar c$  and for a general nuclear charge distribution  $\rho(\mathbf{r})$  the vacuum polarization may

<sup>16</sup>See, for example, L. I. Schiff, *Quantum Mechanics* (McGraw-Hill Book Co., New York, 1955), pp. 331–339.

be written as a correction to the electrostatic energy<sup>17,18</sup>:  $V(\mathbf{r}) + V_p(\mathbf{r})$ . A multipole expansion of  $V_p(\mathbf{r})$  gives as the monopole term the result<sup>19</sup>

$$\phi_p(\mathbf{r}) = (2\alpha e^2/3r)\lambda_e \times \int_0^\infty \bar{\rho}(r')r' \left[ \chi_2\left(\frac{r+r'}{\lambda_e}\right) - \chi_2\left(\frac{|r-r'|}{\lambda_e}\right) \right] dr', \quad (10)$$

where  $\chi_n(\xi)$  is the integral

$$\chi_n(\xi) = \int_1^\infty \frac{1}{z^n} \left(1 + \frac{1}{2z^2}\right) \left(1 - \frac{1}{z^2}\right)^{1/2} \exp(-2\xi z) dz \quad (11)$$

and  $\lambda_e$  is the Compton wavelength of the electron. It is rather unwieldy to use Eq. (10) in actual calculations as it stands. Following Glauber *et al.*,<sup>20</sup> who give an expansion for  $\chi_1$ , we have expanded  $\chi_2$ , with the results

$$\chi_2(\xi) = \sum_{k=0}^{\infty} [a_k(2\xi)^k \exp(-2\xi) + b_k(2\xi)^{2k+1} E_i(2\xi)], \quad (12)$$

where  $E_i(2\xi)$  is the exponential integral

$$\int_1^\infty \frac{\exp(-2\xi z)}{z} dz.$$

Cutting off the expansion at  $a_4$  and  $b_2$  as we have done introduces an error no larger than about 0.01%.

The electronic vacuum polarization is obtained in the present work from a first-order perturbation calculation using the numerically derived wave functions

$$\Delta E_{vp} = \int_0^\infty \phi_p(\mathbf{r}) (F^2 + G^2) dr. \quad (13)$$

The vacuum polarization increases the binding energy of the muon somewhat less than 0.7%. Thus, for the heaviest nuclei, the 1s-level vacuum polarization is on the order of 70 keV.

For the muonic Lamb shift, we use the usual expression to order  $\alpha$  in the form of a potential energy<sup>19,21</sup>:

$$\phi_{LS}(\mathbf{r}) = \frac{4}{3}\alpha e^2 \lambda_\mu^2 \left[ \ln(mc^2/2\Delta E) + \frac{1}{2} - \frac{1}{3} \right] \bar{\rho}(\mathbf{r}), \quad (14)$$

where  $\lambda_\mu$  is the Compton wavelength of the muon and  $\Delta E$  is a certain average of the excitation energy of the muon defined by the Bethe sum.<sup>19,21</sup> We have used  $\bar{\rho}(\mathbf{r})$  instead of  $\rho(\mathbf{r})$  for simplicity, in view of larger uncertainties inherent in Eq. (14). Equation (14) was derived originally to explain the  $2p_{1/2}$ - $2s_{1/2}$  splitting in

electronic hydrogen and is meant to be valid, provided  $Z\alpha \ll 1$ . The condition is not satisfied very well for heavy, high- $Z$  nuclei. However, for heavy muonic atoms there is a saving feature, to the extent that the nuclear charge reduces the effective value of  $Z$  in the critical region  $r \sim \lambda_\mu$ . In Pb, for example, the radius of the nucleus is 7 F, the 1s Bohr radius is 3 F, while  $\lambda_\mu = 1.9$  F.

A second problem occurs with the Bethe sum. We follow Barrett *et al.*<sup>19</sup> and use for  $\Delta E$  the binding energy of the muon for the particular energy level to which the Lamb shift is being applied. These authors estimate that the resulting Lamb shift has a 30% uncertainty, arising principally from  $\Delta E$ .

We calculate the Lamb shift in first-order perturbation. In the region of Pb, the 1s muonic Lamb shift is on the order of  $3.0 \pm 1.0$  keV. The Lamb shift decreases the binding energy.

The energy shift due to the muon anomalous magnetic moment can also be written in the form of a correction to the potential energy. To order  $\alpha$ , this is

$$\phi_m(\mathbf{r}) = -(i\alpha/4\pi)\lambda_\mu [d\phi(\mathbf{r})/dr] \beta \alpha_r, \quad (15)$$

where  $\alpha_r = \mathbf{r} \cdot \boldsymbol{\alpha}/r$ . In first-order perturbation the energy shift is

$$\Delta E_m = -\frac{\alpha}{2\pi} \lambda_\mu \int_0^\infty \frac{d\phi(\mathbf{r})}{dr} F(r) G(r) dr. \quad (16)$$

The anomalous magnetic moment correction as formulated in Eq. (15) also suffers the same uncertainties as the Lamb shift, resulting from the assumption of  $r \gg \lambda_\mu$ . But in the lowest levels where the uncertainty is greatest, the anomalous magnetic moment shift is considerably less than the Lamb shift. It is about  $0.4 \pm 0.1$  keV for the 1s level for nuclei in the vicinity of Pb. The anomalous part also increases fine-structure splittings; in the vicinity of Pb the  $2p$  fine-structure splitting is increased by about 0.4 keV.

Among other possible corrections, the nuclear polarization effect is probably the most important. This has been calculated by many authors with widely different results,<sup>22-26</sup> depending on the nuclear model used. Recently, Cole<sup>25</sup> has calculated, using an average nuclear model, the nuclear polarization due to the giant dipole resonance, and in the vicinity of Pb, his results show an extra binding of the muon of about 5 keV for the 1s level and 1 keV for the  $2p$  levels. Pieper and Greiner,<sup>26</sup> on the other hand, have taken specific nuclei, including  $U^{238}$  and  $Th^{232}$ , and have calculated the nuclear polarization due to the giant monopole, dipole, and quadrupole resonances. They find that the binding is increased by about 1 keV for the 1s and  $2p$  levels. Nuclear polarization effects increase the binding energy by a small amount. However, because of the

<sup>17</sup> E. A. Uehling, Phys. Rev. **48**, 55 (1935); R. Serber, *ibid.* **48**, 49 (1935).

<sup>18</sup> J. Schwinger, Phys. Rev. **75**, 651 (1949).

<sup>19</sup> R. C. Barrett, S. J. Brodsky, G. W. Erickson, and M. H. Goldhaber, Phys. Rev. **166**, 1589 (1968).

<sup>20</sup> R. Glauber, W. Rarita, and P. Schwed, Phys. Rev. **120**, 609 (1960).

<sup>21</sup> H. A. Bethe, L. M. Brown, and J. R. Stehn, Phys. Rev. **77**, 370 (1950); J. D. Bjorken and S. D. Drell, *Relativistic Quantum Mechanics* (McGraw-Hill Book Co., New York, 1964), pp. 177-179.

<sup>22</sup> L. N. Cooper and E. M. Henley, Phys. Rev. **92**, 801 (1953).

<sup>23</sup> W. Lakin and W. Kohn, Phys. Rev. **94**, 787 (1954).

<sup>24</sup> F. Scheck, Z. Physik **172**, 239 (1963).

<sup>25</sup> R. K. Cole, Jr., Phys. Letters **25B**, 178 (1967).

<sup>26</sup> W. Pieper and W. Greiner, Phys. Letters **24B**, 377 (1967).

uncertainties in calculating them they have not been explicitly included in this work.

Other corrections which have been considered<sup>19,22</sup> appear to be negligible for the purposes of this work. In particular, the screening due to atomic electrons appears<sup>19</sup> to produce a shift of only a few eV. The non-electromagnetic (weak) interaction of the muon with the nucleus has been estimated<sup>22</sup> to be on the order of a few eV. The error introduced by using the reduced mass in the Dirac equation has been estimated<sup>19</sup> to be less than 1 keV.

### III. QUADRUPOLE HYPERFINE STRUCTURE

#### A. Bohr-Mottelson Model

The muon binding energies, which include the various corrections discussed in Sec. II, and the eigenfunctions  $\psi_{n\kappa\mu}$  of the Hamiltonian  $H_0(\mathbf{r}, \delta)$ , Eq. (4), form the unperturbed states of the muon in the electrostatic field of the angular-averaged charge distribution of the nucleus. If the charge distribution were spherically symmetric, this would be the end of the story. But the asymmetry of the charge distribution introduces new effects; the unperturbed states will be mixed; unperturbed energy levels will be split and shifted. In this paper only electric quadrupole effects are considered.

The quadrupole term is the next term in the multipole expansion of the electrostatic potential energy  $V(\mathbf{r})$  which contributes anything. It is assumed that the nucleus is rigid with a cylindrically symmetric charge distribution  $\rho(\mathbf{r}_N)$ . The vector  $\mathbf{r}_N$  refers to a coordinate system fixed in the nucleus with the axis of symmetry in the direction of  $z_N$ . Thus, following Willets,<sup>5</sup> the quadrupole term of  $V(\mathbf{r})$  can be written

$$H' = -\frac{1}{2}Q_0e^2f(r)P_2(\cos\theta), \quad (17)$$

where  $\theta$  is the angle between the muon coordinate  $\mathbf{r}$  and the  $z_N$  axis. The intrinsic quadrupole moment  $Q_0$  is defined in terms of the body-fixed quadrupole charge distribution

$$\rho^{(2)}(\mathbf{r}_N) = (3z_N^2 - r_N^2)\rho(\mathbf{r}_N), \quad (18)$$

$$Q_0 = \int \rho^{(2)}(\mathbf{r}_N) d^3r_N. \quad (19)$$

The function  $f(r)$ , called the penetration factor, is

$$f(r) = \frac{1}{r^3} \left( 1 - Q_0^{-1} \int_r^\infty \frac{r_N^5 - r^5}{r_N^3} dr_N \int \rho^{(2)}(\mathbf{r}_N) d\Omega_N \right). \quad (20)$$

The quantity  $H'$  is the quadrupole part of the interaction energy between the muon and the nucleus. The muon coordinates are  $r$ ,  $\theta$ , and  $\phi$ , while the nuclear coordinates are collective, with  $\theta_N$  and  $\phi_N$ , the polar and azimuthal angles of the  $z_N$  axis of the nucleus, in the laboratory frame. There is a third nuclear coordi-

nate,  $\psi_N$ , which is the angular position of the nucleus about the axis of symmetry.

We adopt as our nuclear model for  $U^{238}$  and  $Th^{232}$  the Bohr-Mottelson collective model for highly deformed nuclei.<sup>27</sup> Nuclei in the region of  $155 < A < 185$  and  $A > 230$  display in their spectra rotational sequences indicating permanent intrinsic deformations. Usually the spacings of the rotational levels show the regularity that would be expected from the energy levels of the rotations of the quantum-mechanical symmetric top, thus indicating that the nucleus has an axis of symmetry and acts like a rigid rotator. In this model the nuclear state is described by three quantum numbers:  $I$ , the total angular momentum of the nucleus;  $\Lambda$ , the angular momentum component along the  $z$  axis in the laboratory frame; and  $K$ , the component along the nuclear axis of symmetry. For the lowest rotational states  $K$  is constant and is equal to the ground-state spin. In the case of even-even nuclei, whose ground-state spin is zero,  $K=0$ .

The rotational Hamiltonian of the nucleus is that of a quantum-mechanical rigid rotator  $H_{rot}$ ; for even-even nuclei its eigenvalues are the rotational levels:

$$E_I = (\hbar^2/2\mathcal{I})[I(I+1)], \quad (21)$$

where  $\mathcal{I}$  is the moment of inertia. The sequence of states is  $I=0, 2, 4, 6$ , etc. The eigenfunctions of  $H_{rot}$  are the spherical harmonics:

$$\psi_{IK}^\Lambda = (2\pi)^{-1/2} Y_{I\Lambda}(\theta_N, \phi_N). \quad (22)$$

For the present purposes, it is not necessary to consider the more detailed aspects of the Bohr-Mottelson model, such as vibrational modes. It is sufficient to consider, in addition to the ground state with  $I=0$ , only the first two excited states with  $I=2$  and  $I=4$ .

It is of interest to see how well the rotational levels of  $U^{238}$  and  $Th^{232}$  satisfy the criteria of a rigid symmetric rotator whose energy levels are given by Eq. (21). According to this equation, the energy levels of the first two excited states are given by  $E_2=3\hbar^2/\mathcal{I}$  and  $E_4=10\hbar^2/\mathcal{I}$ . By defining a quantity  $\epsilon$  as

$$\epsilon = 10E_2/3E_4 - 1 \quad (23)$$

and using the experimental values for  $E_2$  and  $E_4$  in calculating  $\epsilon$ , the departure from the ideal rigid rotator will be revealed to some extent. Any small departure of  $\epsilon$  from zero is an expected small centrifugal stretching increase in the moment of inertia. Table I gives the experimental values of  $E_2$  and  $E_4$  and the resulting values of  $\epsilon$  for  $U^{238}$  and  $Th^{232}$ . The results of Table I show that, at least for the lowest two excited states, the  $U^{238}$  and  $Th^{232}$  nuclei are evidently very well described by the rotational model.

<sup>27</sup> A. Bohr and B. R. Mottelson, Kgl. Danske Videnskab. Selskab, Mat.-Phys. Medd. **27**, No. 16 (1953).

### B. Matrix Elements

The total Hamiltonian of the muon plus nucleus system up to the quadrupole interaction term is

$$H = H_0 + H_{\text{rot}} + H'. \quad (24)$$

The muon states are found by solving the Dirac equation numerically, while the nuclear energy levels of  $U^{238}$  and  $Th^{232}$  are taken from experiment.<sup>28</sup> Various corrections, as discussed above, are added to the muon energies.

In the coupled representation the unperturbed Hamiltonian  $H_0 + H_{\text{rot}}$  has as eigenfunctions the eigenfunctions of total angular momentum  $F$ :

$$\psi_{FM, n\kappa IK} = \sum_{\mu\Lambda} C(jIF; \mu\Lambda M) \psi_{n\kappa}^{\mu} \psi_{IK}^{\Lambda}, \quad (25)$$

where  $C(jIF; \mu\Lambda M)$  is the usual Clebsch-Gordan<sup>29</sup> coefficient. In this representation the matrix elements of  $H$  are

$$\begin{aligned} & (FM, n\kappa IK | H | FM, n'\kappa' I'K') \\ &= (E_{n\kappa} + E_{IK}) \delta_{nn'} \delta_{\kappa\kappa'} \delta_{II'} \delta_{KK'} - \frac{1}{2} Q_0 e^2 \frac{4}{5} \pi (2j+1)^{1/2} \\ & \quad \times (2I+1)^{1/2} W(jIj'I'; F2) (-1)^{j+I'-F} \\ & \quad \times (n\kappa || f(r) Y_2(\theta, \phi) || n'\kappa') \\ & \quad \times (IK || Y_2(\theta_N, \phi_N) || I'K'), \quad (26) \end{aligned}$$

where the  $W$  symbol is the Racah coefficient and the double-barred symbols are the reduced matrix elements.

All the quantities which depend on a choice of a specific charge distribution for the nucleus are contained in  $Q_0$  and the function  $f(r)$  in the muon reduced matrix element. These two quantities are combined to give what is termed here the "quadrupole energy." Following Wilets<sup>5</sup> (except for the sign), the quadrupole energy is defined as

$$E(n\kappa, n'\kappa') = +\frac{1}{10} Q_0 e^2 \int_0^{\infty} f(r) (F_{n\kappa} F_{n'\kappa'} + G_{n\kappa} G_{n'\kappa'}) dr. \quad (27)$$

TABLE I. First two rotational levels of  $U^{238}$  and  $Th^{232}$ .<sup>a</sup> The quantity  $\epsilon$ , defined by Eq. (23), measures the amount of departure of the first two nuclear levels from those of an ideal rigid rotator with a symmetry axis.

Quantity	$U^{238}$	$Th^{232}$
$E_2$ (keV)	44.7±0.2	49.75±0.25
$E_4$ (keV)	147.7±2.0	162.80±2.0
$\epsilon$ (%)	0.9±1.4	1.90±1.4

<sup>a</sup> Taken from Ref. 28.

<sup>28</sup> F. S. Stephens, Jr., R. M. Diamond, and I. Perlman, Phys. Rev. Letters **3**, 435 (1959).

<sup>29</sup> M. E. Rose, *Elementary Theory of Angular Momentum* (John Wiley & Sons, Inc., New York, 1957), Eq. (6.21). The notation of this reference is used in the present work.

All the physics of the quadrupole interaction is contained in the  $E(n\kappa, n'\kappa')$ ; the remaining factors of Eq. (26) are just the coefficients of the angular momentum algebra which are tabulated in many places.<sup>30</sup> Thus, the matrix elements of the total Hamiltonian are, after collecting all the factors,

$$\begin{aligned} & (FM, n\kappa IK | H | FM, n'\kappa' I'K') \\ &= (E_{n\kappa} + E_{IK}) \delta_{nn'} \delta_{\kappa\kappa'} \delta_{II'} \delta_{KK'} \\ & \quad - 5(-1)^{F-I'+l-1/2} E(n\kappa, n'\kappa') \delta_{KK'} \\ & \quad \times [(2j+1)(2j'+1)(2l+1)(2l+1)]^{1/2} \\ & \quad \times C(l2l'; 000) C(l2l'; -K, 0, -K) \\ & \quad \times W(jIj'I'; F2) W(lj'l'j'; \frac{1}{2}2). \quad (28) \end{aligned}$$

For a given muonic atom all the quantities in Eq. (28) are known except the unperturbed atomic energies  $E_{n\kappa}$  and the quadrupole energies  $E(n\kappa, n'\kappa')$ . These remain as parameters to be determined by fitting the observed spectrum. Once they are determined, we seek, from a solution of the Dirac equation (with corrections), a consistent set of nuclear shape parameters.

The assumption made in the Bohr-Mottelson model that the nucleus keeps the same shape in the excited rotational states means that the quadrupole energy depends only upon the muon states. The actual muonic spectra seen in experiment may depart from this to some extent; if the departure is due to breakdown of the assumption of a rigid nucleus, perhaps due to the mixing in of vibrational states or individual particle excitations, the breakdown may be taken care of formally, following Jacobsohn,<sup>6</sup> by introducing "nuclear parameters"  $\epsilon_{II'}$  into the quadrupole energy:

$$E(n\kappa I, n'\kappa' I') = \epsilon_{II'} E(n\kappa, n'\kappa'), \quad (29)$$

where, by definition,  $\epsilon_{00} = 1$ , since  $Q_0$  is the quadrupole moment of the ground state. The quantity  $Q_{II'} \equiv \epsilon_{II'} Q_0$  could then be called the "dynamic quadrupole moment." It reflects the change in shape of the nucleus in leaving the ground state.

### C. Energy Levels

In the present work only principal transitions  $4f \rightarrow 3d$ ,  $3d \rightarrow 2p$ , and  $2p \rightarrow 1s$  were analyzed in both  $U^{238}$  and  $Th^{232}$ . Off-diagonal matrix elements connecting states with different  $n$  or  $l$  are small and were ignored. Thus, only the muonic states  $2p$ ,  $3d$ , and  $4f$  were considered and each was handled separately. For each  $nl$  muonic state several matrices appear, one for each of the possible values of  $F$ . Each matrix, having a given  $F$ ,  $n$ , and  $l$ , was separately diagonalized.

For a given muonic state  $nl$ , except  $s$  and  $p$  states, three quadrupole energies  $E(n\kappa, n'\kappa')$  describe the state. In general, the three quadrupole energies differ by less

<sup>30</sup> M. Rotenberg, R. Bevens, N. Metropolis, and J. K. Wooten, Jr., *The 3n-j Symbols* (The MIT Press, Cambridge, Mass., 1959).

than 15%. For the  $2p$  state, in which the quadrupole energy is by far the largest, the two quadrupole energies that occur differ by about 1%. Also, the ratios of the three quadrupole energies are calculated to be almost constant over wide ranges of nuclear charge distribution parameters. For this reason, one quadrupole energy, the one off-diagonal in  $j$ , and two ratios are chosen to describe the quadrupole interaction. The two ratios  $\eta_1$  and  $\eta_2$  are then defined as

$$\eta_1 = \frac{E(nl, l-\frac{1}{2}; nl, l-\frac{1}{2})}{E(nl, l-\frac{1}{2}; nl, l+\frac{1}{2})},$$

$$\eta_2 = \frac{E(nl, l+\frac{1}{2}; nl, l+\frac{1}{2})}{E(nl, l-\frac{1}{2}; nl, l+\frac{1}{2})}. \quad (30)$$

In fitting the spectra it is an excellent approximation to assume that  $\eta_1$  and  $\eta_2$  are constant. This procedure was adopted in this paper.

The  $I=4$  rotational level of  $\text{Th}^{232}$  and  $\text{U}^{238}$  is around 150 keV, which is on the same order of magnitude as the  $2p$  splitting and  $2p$  quadrupole energy. For this reason it is necessary to include the  $I=4$ , as well as the  $I=0$  and 2 rotational states, in the  $2p$  Hamiltonian. For the  $3d$  and  $4f$  levels, only the  $I=0$  and 2 states are needed. Actually, the hfs in the  $4f$  level could be done in first-order perturbation or just ignored; however, it turned out that it took very little extra work to include it.

After diagonalizing a Hamiltonian matrix of given  $n'lF$ , the mixed states which occur are written as

$$\Psi_{n'lF}^i = \sum_{jI} C_{FnljI}^i \Psi_{FnljI}, \quad (31)$$

where  $lj$  is now written in place of  $\kappa$ , and the nuclear quantum number  $K$ , which is zero everywhere, is suppressed.

The eigenvalues of the Hamiltonian are the energy states of the total system of muon and nucleus; these eigenvalues are denoted by  $E_{n'lF}^i$ . The  $2p$  energy states of  $\text{Th}^{232}$  and  $\text{U}^{238}$  are greatly split and shifted as shown in Fig. 8; the mixing is so great that  $j$  and  $I$  are not even approximately good quantum numbers. However,  $2p$  is still a good description of the state because of the negligible amount of mixing in from other  $nl$  states.

#### D. Line Intensities

The muonic x rays are emitted when the muon nucleus system undergoes a transition from the state  $n'l'F'i$  to the state  $nlFk$ . Only the electric dipole radiation is of any importance here. The usual selection rules,  $\Delta F=0, \pm 1$ , except  $0 \rightarrow 0$  apply, and since only the principal lines are dealt with, the further restrictions  $\Delta l = -1$  and  $\Delta n = -1$  pertain.

In the nonrelativistic dipole approximation the transition probability from initial state  $n'l'F'i$  to final state

$nlFk$  is proportional to

$$I_{ik}(n'l'F' \rightarrow nlF) = E_{ik}^3 \sum_{MM'} | \langle nlFMk | \mathbf{r} | n'l'F'M'i \rangle |^2, \quad (32)$$

where  $E_{ik} = E_{n'l'F',i} - E_{nlF,k}$  and  $\mathbf{r}$  is the muon coordinate. Again, by using theorems<sup>29</sup> dealing with spherical tensors, this becomes

$$I_{ik}(n'l'F' \rightarrow nlF) = E_{ik}^3 (2l+1)(2F+1)(2F'+1) | C(l1l'; 000) |^2 \\ \times \left| \sum_{jj'I} (-1)^{i+j'-I} (2j+1)^{1/2} (2j'+1)^{1/2} \right. \\ \times \langle nlj | \mathbf{r} | n'l'j' \rangle C_{FnljI}^k \\ \left. \times C_{F'n'l'j'I}^i W(lj'l'j'; \frac{1}{2}1) W(jj'FF'; 1I) \right|^2. \quad (33)$$

In this work the sequence of transitions  $4f \rightarrow 3d \rightarrow 2p \rightarrow 1s$  is studied. Corresponding to each successive transition is a group of lines, the  $M$ ,  $L$ , and  $K$  lines, respectively, each widely separated in energy. Within each group the relative intensity as well as the absolute energy of each hfs line was calculated for comparison with experiment.

The relative intensity of a transition from the initial state  $n'l'F'i$  to the final state  $nlFk$  is the product of the population of the initial state and the branching ratio of the transitions to the final state. For a statistically populated initial state the population is just  $2F'+1$ . The branching ratio is just the fraction of transitions which lead to a specified final state. For the principal lines we include only  $n=n'-1$ ,  $l=l'-1$  and neglect transitions to states with other values of  $nl$ . The population of the final state  $nlFk$  must be proportional to the sum of the intensities reaching it from higher states. For the purposes of the present work it is a good approximation to consider that only states with  $n'=n+1$ ,  $l'=l+1$  feed the states with  $nl$ . Cross-over transitions such as  $4d \rightarrow 2p$  do occur, but with intensities small compared with  $3d \rightarrow 2p$ .

The  $4f$  level is assumed to be statistically fed from above, from states which have no quadrupole interaction and in which the nucleus is in its ground state. The dipole transitions leave the nuclear state unchanged, so that the promotion to states of higher nuclear spin comes initially in the  $f$  level due to quadrupole mixing there. In practice there is very little mixing in the  $f$  level. The population of the  $F' = \frac{7}{2}$  and  $\frac{5}{2}$  levels differ from  $2F'+1$  by less than 1%; see Fig. 10. The quadrupole mixing is much larger in the lower atomic states, with the result that an appreciable fraction of the nuclei find themselves in the higher rotational states by the time the  $1s$  muonic level is reached.

#### IV. MEASUREMENTS

Measurements were made using a large (17-cm<sup>3</sup>) Ge(Li) detector of coaxial design. Such a large detec-

tor offers greater data collection efficiency at some loss of resolution and with some asymmetry in the line shape.

Pulse-height analysis was done with a 4096-channel analog-to-digital converter of high stability in conjunction with a PDP-8 computer. This combination made it possible to provide a number of functions which served to extend the dynamic range of the pulse-height measurement and to provide a high degree of stability, so that data could be collected for many days without appreciable broadening of the x-ray peaks. Moreover, a variety of spectra could be recorded simultaneously.

Measurements were always made with two targets. One of these was a standard  $Pb^{206}$  sample, the other was a sample of either  $Th^{232}$  or  $U^{238}$ . The  $Pb^{206}$  data were recorded simultaneously with the  $Th^{232}$  or  $U^{238}$  data, through the same detector and analysis system. The  $Pb^{206}$  data provided the standard line shapes used in peak fitting, and an absolute energy scale. It also served as a means of checking drifts and other malfunctions.

Muons from the muon channel of the University of Chicago synchrocyclotron were stopped and identified by the telescope in one of two targets as shown in Fig. 1. The muonic x rays were measured by a Ge(Li) coaxial diode located at  $90^\circ$  from the axis of the muon beam. Surrounding the diode was a split annulus of NaI with each half optically isolated. The x-ray data (prompt events) from the germanium detector were run in three modes: (i) all diode events, (ii) diode in anticoincidence with the annulus in order to reduce the Compton background, and (iii) a triple coincidence between the diode and both halves of the annulus in order to isolate double-escape peaks with greatly reduced background.

After being suitable amplified, the diode pulse was analyzed by a 4096-channel (12-bit) analog-to-digital converter (ADC) whose gain was automatically sta-

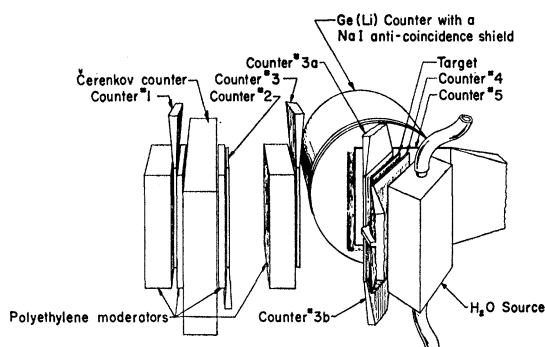


FIG. 1. Muon telescope. The muon beam came from the left. Counters 1-3 defined the beam. Counters 3a and 3b indicated which target the muon struck. Counter 4, in anticoincidence, indicated the stopping of the muon in the targets. Counter 5 vetoed charged particles that stopped in the Ge counter. The Čerenkov counter was used to veto electrons in the beam. The polyethylene was used as absorber to remove pions and slow down the muons.

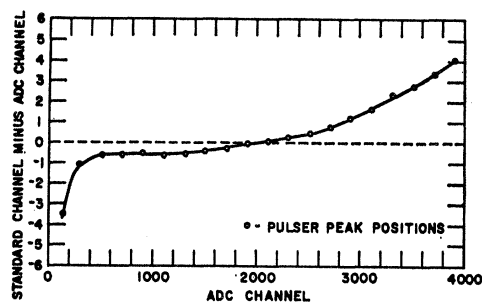


FIG. 2. Deviation from linearity of the ADC and linear amplifier using the 20 pulser peaks and their DVM readings. The standard channel that corresponds to the ADC channel is really the DVM reading of the ADC channel scaled by the factor  $C_{10}/V_{10}=0.4012$  channels/mV, where  $C_{10}$  is the ADC channel position of the 10th pulser peak and  $V_{10}$  is its DVM voltage reading.

bilized by two independent precision pulsers. Each digitized event was stored in an on-line computer system by taking the digitized event, treating it as an address, and adding 1 to the contents of the appropriate memory location. Tag logics determined which target and which mode the event belonged to. Furthermore, the time of each diode event relative to the muon stop was digitized and used by the on-line computer to separate prompt from delayed events. Events of mode (i) were stored for all 4096 channels of the ADC. With the gain of the system set at 1.6 channels/keV, the spectra of mode (i), called the  $X$  spectra, had a range from about 150 keV, the noise threshold, to 6.4 MeV.

Energy calibration lines using several standard  $\gamma$ -ray sources were simultaneously fed into the system. Also fed in simultaneously was the output of a variable-amplitude precision pulser which automatically stepped through 20 voltage settings every 10 min or so. Each pulser setting was monitored by a digital voltmeter whose voltage readings were also fed into the computer system. Thus, the linearity and stability of the system were constantly being checked. The sources and pulser data were brought into the system under conditions similar to those of the x-ray data by employing a beam monitor which limited data collection to beam burst times. This was done to limit the possibility of a systematic shift between x-ray data and the source and pulser data. A pile-up gate was incorporated to assure ample time in the measurement of each pulse height free from the tail of a preceding pulse. A more complete description of the apparatus is found in Ref. 15.

## V. DATA REDUCTION

### A. Peak Fitting

The positions and intensities of the peaks in a spectrum were found by fitting to the data an empirical line shape whose mathematical form was suggested by the following line-shape characteristic: The line shape generally showed a low-energy tail at higher energies,

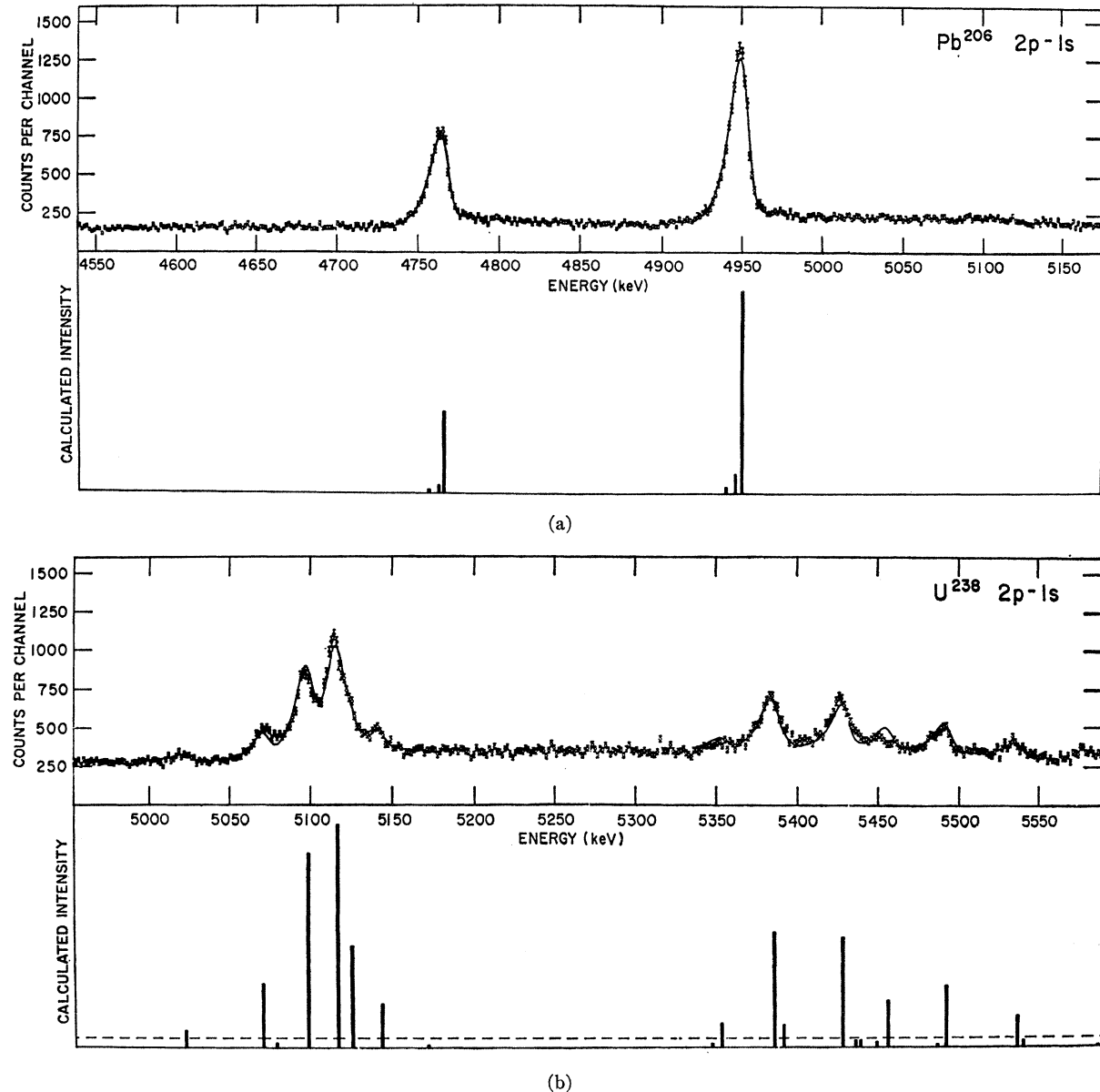


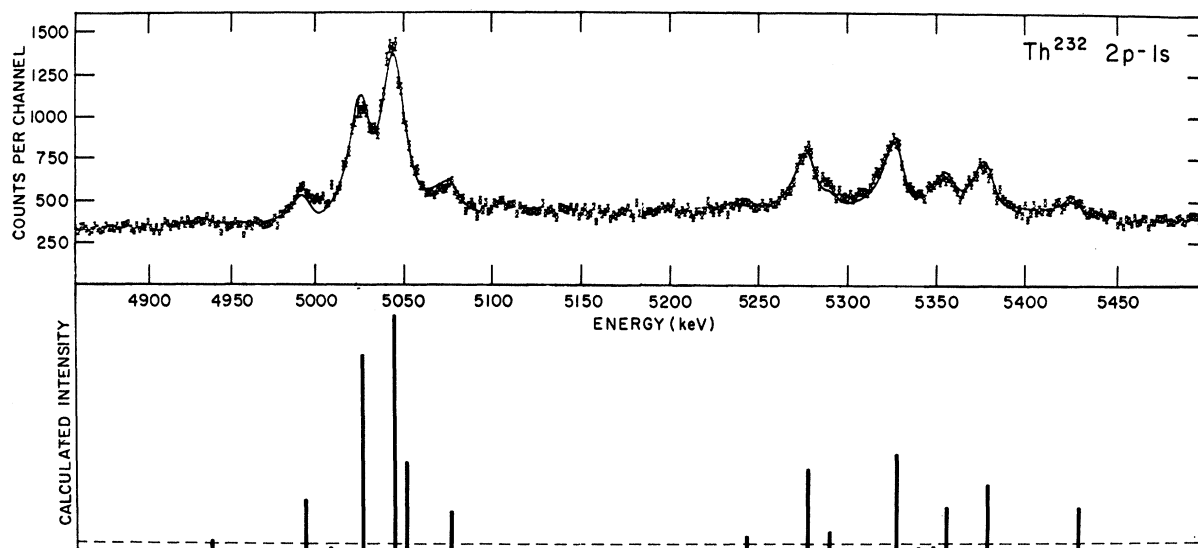
FIG. 3. The  $2p \rightarrow 1s$  double-escape spectra of  $\text{Pb}^{206}$ ,  $\text{U}^{238}$ , and  $\text{Th}^{232}$  showing the best fits to the data. All 22 lines predicted by the hfs formalism are shown below the  $\text{U}^{238}$  and  $\text{Th}^{232}$  spectra. Only lines intense enough to be above the horizontal dashed line were used in the fit. The remaining lines constituted 3.4% for  $\text{U}^{238}$  and 2.6% for  $\text{Th}^{232}$  of the total intensity. The  $\chi^2$  values for the fitted regions of the spectra are  $\chi^2 = 2.04$  per degree of freedom for  $\text{U}^{238}$  with 233 degrees of freedom and  $\chi^2 = 1.99$  per degree of freedom for  $\text{Th}^{232}$  with 233 degrees of freedom. The two satellite peaks used in the  $\text{Pb}^{206}$  fit are from the  $\text{Pb}^{207}$  and  $\text{Pb}^{208}$  isotopic impurities in the  $\text{Pb}^{206}$  target. All three spectra were fitted with the same line-shape parameters.

while at energies below 500 keV the peaks were fairly Gaussian. Thus, in the mathematical form it has been assumed that the basic response of the apparatus was Gaussian, but that regions of the Ge detector were less efficient in charge collection, and hence threw counts from the Gaussian into a low-energy tail.

The line shape was taken to be made up of two parts: a fraction  $1-f_1$  having the Gaussian form and a fraction  $f_1$  having an exponential tail folded into the same

Gaussian. In these terms the number of counts in the peak at channel  $C$  may be written

$$N_p(C) = N_0 \left( (1-f_1) \exp[-\lambda(C-C_0)^2] + f_1 \beta \int_C^\infty \exp[-\lambda(C'-C_0)^2 - \beta(C'-C)] dC' \right), \quad (34)$$



(c)

where  $C_0$  is the central channel of the undistributed peak and where  $N_0$  is its amplitude.

The channel position of the Gaussian  $C_0$  was not used to define the peak position; rather, the position of the top of the fitted line shape, the channel where  $dN_p(C)/dC=0$ , was chosen. This was done since, for a well-fitted asymmetric peak, the fit at the top of the peak is an invariant property of the data, no matter what reasonable functional form  $N_p(C)$  is assumed, whereas  $C_0$  is a parameter for a specific function, Eq. (34), and thus may not be well defined by the data. The line shape chosen here is a reasonable description, not an exact one. But the top of the line position should be insensitive to this choice. However, the statistical error in the peak position was taken to be the same as the statistical error in determining  $C_0$ .

The automatic 20-step pulser together with digital-voltmeter readings (DVM) for the amplitude of each pulser peak were used to correct any nonlinearity in the electronics. Between channels 300 and 4000 this nonlinearity amounted to one part in 1000. With pulser peaks taken in continuous succession while the data were being gathered it was possible to convert any set of observed channels to a standard linearized set by referring to the DVM readings. Thus, the channels  $C_i$  at which the pulser peaks appear are converted into a standard channel using the relation

$$C_i^{(s)} = (C_{10}/V_{10}) V_i, \quad i=1, 20. \quad (35)$$

Other channels are made standard by interpolation. Figure 2 shows a plot of the deviation from linearity for a series of runs during the experiment.

### B. Energy Calibration

Throughout most of the experiment the second target consisted of an almost isotopically pure sample of  $Pb^{206}$ .

A large amount of  $Pb^{206}$  data were accumulated to determine the energies of the principal transitions accurately. Once this was done, the  $Pb^{206}$  lines served to energy calibrate the  $U^{238}$  and  $Th^{232}$  spectra. Figures 3-5 show part of the  $Pb^{206}$  spectrum used for the calibration.

Nine  $Pb^{206}$  spectra were obtained throughout the experiment. Each spectrum consisted of from 2 to 10 individual runs. One  $Pb^{206}$  spectrum had as the second target  $U^{238}$ ; another had  $Th^{232}$ . For each spectrum the  $K$ ,  $L$ , and  $M$  lines of  $Pb^{206}$  were fitted with the line shape described in Sec. V A. All the fitting was done in the  $X$  spectrum. The  $Pb^{206}$  target used was not quite isotopically pure. It had 8.48% of  $Pb^{207}$  and 2.73% of  $Pb^{208}$  as the principal contaminations. Correction for these impurities was made by fitting each of the  $K$  and  $L$  lines with three peaks with the intensity of each peak made proportional to the isotopic abundance and the spacings set equal to the measured<sup>15</sup> isotope shifts.

The Ge detector and DVM itself were nonlinear to some extent. For the conversion from standard channel to energy it was sufficient to use a quadratic form:

$$E = a_0 + a_1 C + a_2 C^2, \quad (36)$$

where  $E$  is the energy in keV and  $C$  now stands for the standard channel. For a given spectrum the  $E-C$  coefficients  $a_0$ ,  $a_1$ , and  $a_2$  were found by a least-squares fit using several peaks whose standard channels have been found by line-shape fitting and whose absolute energies or energy differences are known. Once the  $E-C$  coefficients were known, the absolute energies of other fitted peaks of the same spectrum were calculated.

The  $E-C$  coefficients of each  $Pb^{206}$  spectrum were found by the least-squares fit to Eq. (36), using five  $\gamma$ -ray source peaks, whose peaks were also line-shape-fitted and whose energies are well known, and using

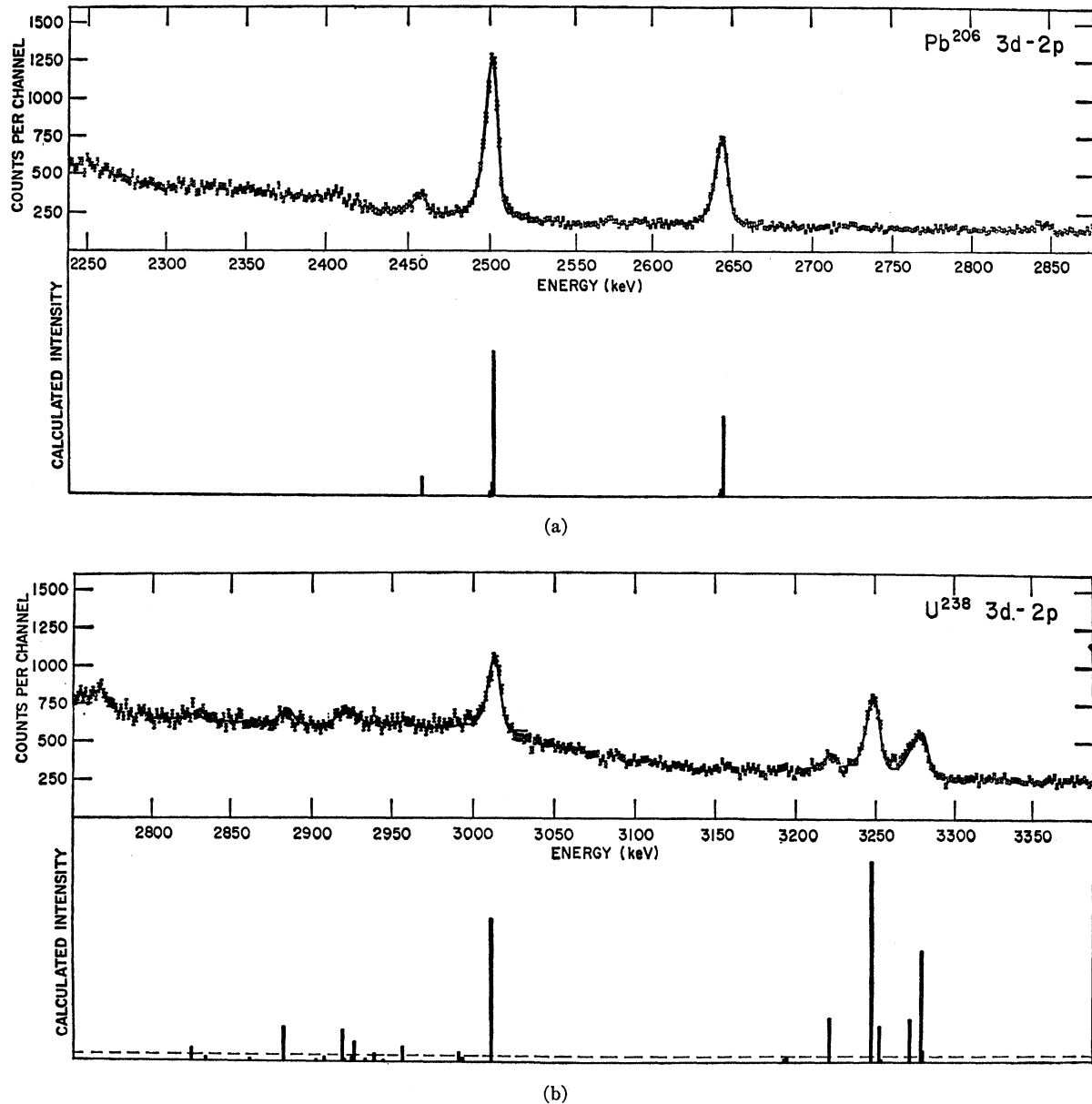


FIG. 4. The  $3d \rightarrow 2p$  full-energy spectra of  $\text{Pb}^{206}$ ,  $\text{U}^{238}$ , and  $\text{Th}^{232}$  showing the best fit to the data. Many of the 66 lines predicted by the hfs formalism are shown below the  $\text{U}^{238}$  and  $\text{Th}^{232}$  spectra. Only lines intense enough to be above the horizontal dashed line were used in the fit. The remaining lines constituted 6.8% for  $\text{U}^{238}$  and 4.5% for  $\text{Th}^{232}$  of the total intensity. The  $\chi^2$  values for the fitted regions of the spectra are  $\chi^2 = 1.62$  with 205 degrees of freedom for  $\text{U}^{238}$  and  $\chi^2 = 1.89$  with 179 degrees of freedom for  $\text{Th}^{232}$ . The  $\text{Pb}^{206}$   $3d_{3/2} \rightarrow 2p_{3/2}$  transition was not fitted with the two extra satellite peaks corresponding to the two isotopic impurities since this peak is so weak. All three spectra were fitted with the same line-shape parameters.

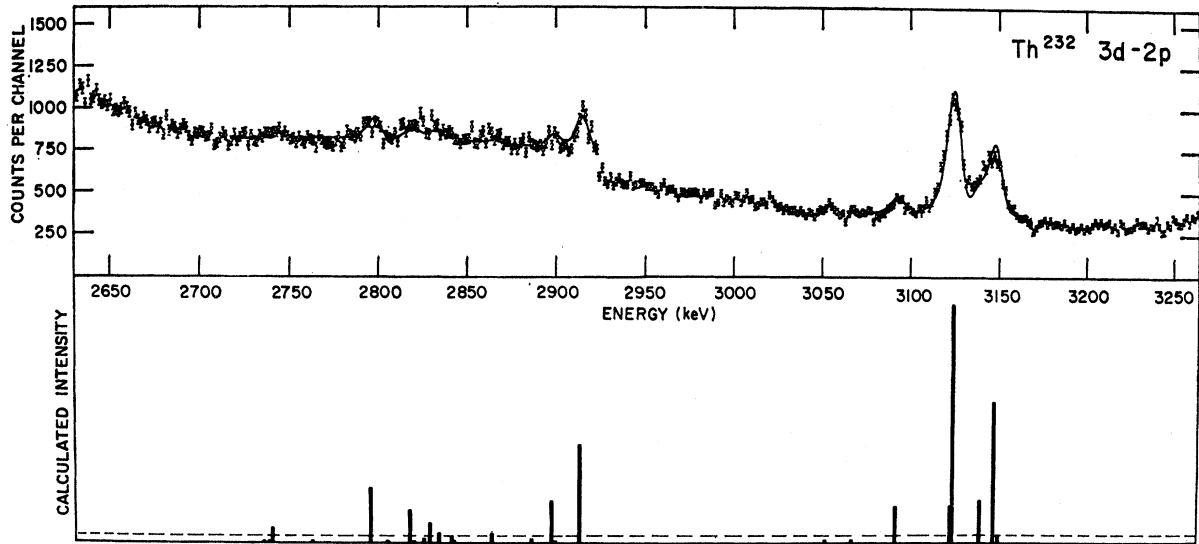
the precisely known energy differences between the double-escape, single-escape, and full-energy peaks in the  $K$  and  $L$  lines. The double-escape peak  $L$  lines of the  $\text{Pb}^{206}$  lines were not used because of a local non-linearity in the system that shifted these peaks by about 1 keV.

The  $\text{Pb}^{206}$  energies of each summed spectrum were calculated from the  $E-C$  coefficients and all the energies of a given line were averaged. For the average,

$m_e c^2 = 511.01$  keV was added to single-escape peaks and  $2m_e c^2 = 1022.02$  keV added to double-escape peaks. The  $\text{Pb}^{206}$  energies found by this analysis were then used in the  $\text{U}^{238}$  and  $\text{Th}^{232}$  energy calibrations.

## VI. ANALYSIS

The  $K$ - and  $L$ -line spectra of the deformed nuclei  $\text{Th}^{232}$  and  $\text{U}^{238}$  are strikingly more complex than those



(c)

of a spherical nucleus like  $Pb^{206}$ . This is apparent from Fig. 3, which shows the  $2p \rightarrow 1s$  transitions (in double escape) for  $Pb^{206}$ ,  $Th^{232}$ , and  $U^{238}$ . The complexity is due to the large hfs splitting in the  $2p$  state. Appreciable hfs splitting occurs also in the  $3d$  state, which makes the  $3d \rightarrow 2p$  transitions even more complicated. The splitting in the  $3d$  state has an appreciable effect on the  $M$  lines ( $4f \rightarrow 3d$ ). What normally appears like a doublet in spherical nuclei shows up here as a triplet.

The  $2p \rightarrow 1s$ ,  $3d \rightarrow 2p$ , and  $4f \rightarrow 3d$  spectra of  $U^{238}$  and  $Th^{232}$  consisted of groups of lines which were fitted using for each line the empirical line shape described by Eq. (34). The channel position  $C_0$  and the amplitude  $N_0$  of each line of appreciable intensity in the group was calculated using the hfs formalism described in Sec. III. The fine-structure splittings and the quadrupole energies (and background levels) were used as parameters and varied until a best fit to the spectra was

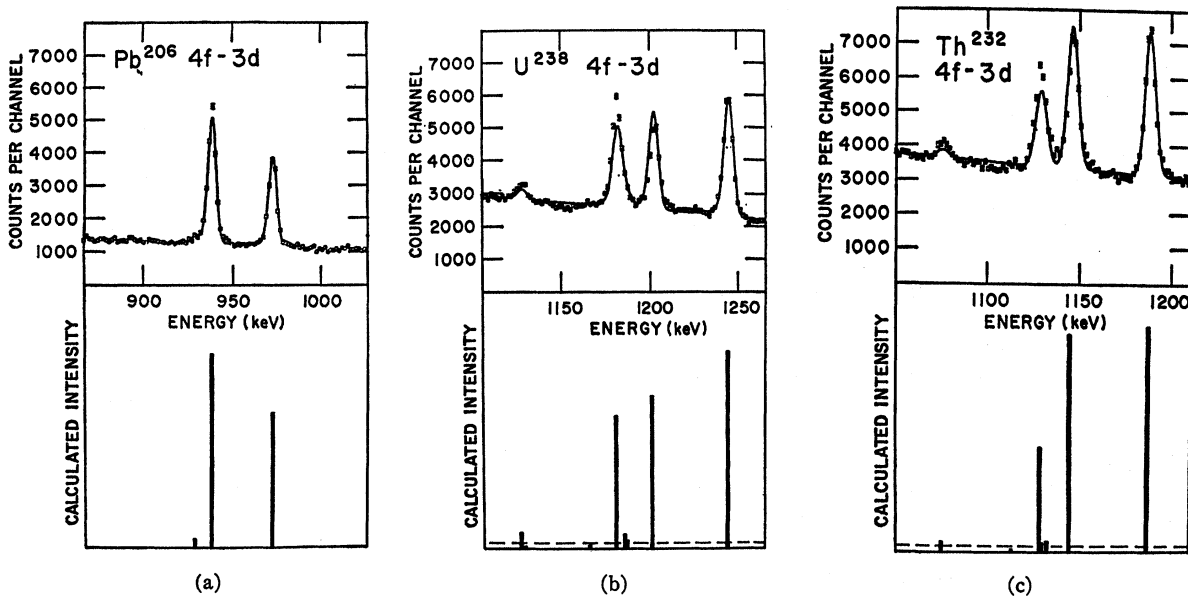


FIG. 5. The  $4f \rightarrow 3d$  full-energy spectra of  $Pb^{206}$ ,  $U^{238}$ , and  $Th^{232}$  showing the best fit to the data. Many of the 42 lines predicted by the hfs formalism are shown below the  $U^{238}$  and  $Th^{232}$  spectra. Only lines intense enough to be above the horizontal dashed line were used in the fit. The remaining lines constituted 1.8% for  $U^{238}$  and 1.2% for  $Th^{232}$  of the total intensity.  $\chi^2 = 9.98$  with 92 degrees of freedom for  $U^{238}$  and  $\chi^2 = 9.03$  with 92 degrees of freedom for  $Th^{232}$ . No satellite peaks were used in the  $Pb^{206}$  fit since the isotope shift was ignored. The three spectra were fitted using different line-shape parameters.

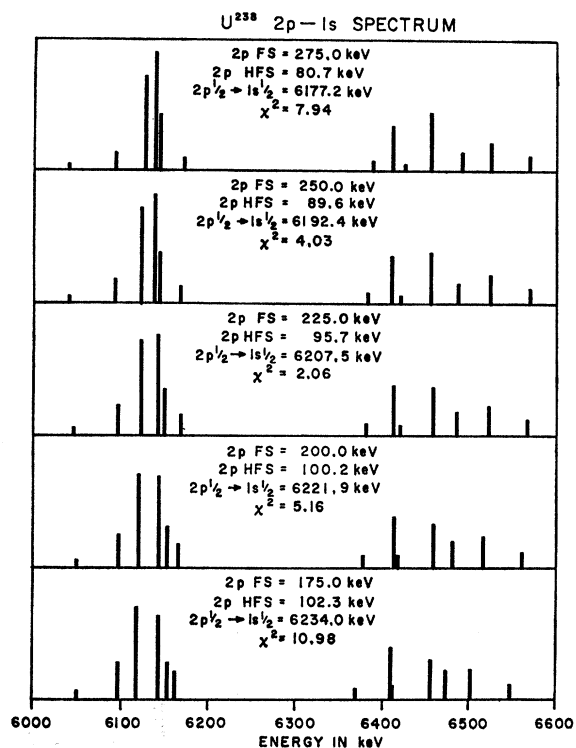


FIG. 6. The  $U^{238}$   $2p \rightarrow 1s$  spectrum showing the principal hfs lines for various  $2p$  fine-structure splittings ranging from 175 to 275 keV. The  $2p$  hfs quadrupole energy and the unperturbed  $2p_{1/2} \rightarrow 1s_{1/2}$  absolute energy were chosen for each  $2p$  fine-structure splitting to give the best fit to the data. The  $\chi^2$  is the chi squared per degree of freedom with 234 degrees of freedom.

obtained (Fig. 6). The rotational energies of the nucleus were fixed at values determined by other work<sup>31</sup>.

Not all the lines obtained from the hfs formalism were used in making the fits. The lines whose cumulative contribution to the total intensity came to not more than about 5% were treated as part of the background. The fits obtained used about a dozen lines in each  $K$  and  $L$  spectrum and six lines in each  $M$  spectrum.

In calculating the hfs splitting, nuclear states up to  $I=4$  were included for the  $2p$  level (Figs. 7 and 8). Because of the small amount of mixing of  $I=4$  in the  $3d$  level, it was not necessary to go higher than  $I=4$  for the  $2p$  level, or higher than  $I=2$  for the  $3d$  and  $4f$  levels (Figs. 9 and 10).

For each muon state of given  $l > 0$  there is a fine-structure splitting and three quadrupole energies [except that the quadrupole energy  $E(p_{1/2}, p_{1/2})$  does not enter]. Only one of the quadrupole energies was varied in searching for the best fit to the data. The other

<sup>31</sup> The rotational levels actually used in the analysis were the calculated ones of Ref. 26. These calculated values are  $E_2=44.7$  keV and  $E_4=147.6$  keV for  $U^{238}$ , and  $E_2=50.1$  keV and  $E_4=163.7$  keV for  $Th^{232}$ . These values are not more than about 1 standard deviation from the experiment values shown in Table I and introduce no appreciable error in the analysis.

quadrupole energies were kept in constant ratio to this one. These ratios, defined by Eq. (30), are listed in Table II. They were determined by calculation using wave functions obtained from a solution of the Dirac equation with a preliminary set of nuclear parameters. This method serves because the ratios are close to unity and nearly constant over a wide range of nuclear shape parameters. The transition matrix elements  $(nlj | r | n'l'j')$  used in calculating the relative intensities of the hfs components were handled in a similar way, since the calculated intensities depend very weakly on these matrix elements.

For a given  $n'l' \rightarrow nl$  transition, the relative positions of the hfs peaks are determined by the fine-structure splittings and the quadrupole energies of both  $n'l'$  and  $nl$  levels, as well as the nuclear rotational energies. One more energy was used to define the absolute position of the group. These were chosen to be the unperturbed  $2p_{1/2} \rightarrow 1s_{1/2}$ ,  $3d_{3/2} \rightarrow 2p_{1/2}$ , and  $4f_{5/2} \rightarrow 3d_{3/2}$  energies for the  $K$ ,  $L$ , and  $M$  transitions, respectively.

On the other hand, the intensities are determined not only by the properties of the levels between which the transition takes place, but also by the way in which the upper level is filled. In practice, the cascade is followed down from the  $4f$  level. However, the initial population of the upper states is kept fixed at a value determined by a preliminary analysis of what happened in the earlier part of the cascade.

We have already pointed out that the intensities were calculated assuming a statistically populated  $4f$  level and that the transition followed the cascade  $4f \rightarrow 3d \rightarrow 2p \rightarrow 1s$ . Both assumptions are only approximately true. In particular, for example, the higher  $d$

TABLE II. Ratios of the quadrupole energies and transition matrix elements that were fixed in the fits to the spectra. The numbers in parentheses are the ratios found by solving the Dirac equation, using the nuclear parameters that give the best fit to the data. The  $(nlj | r | n'l'j')$  are in F.

Quantity	$U^{238}$	$Th^{232}$
$\eta_2(2p)$	1.011(1.011)	1.009(1.009)
$\eta_1(3d)$	1.143(1.142)	1.140(1.141)
$\eta_2(3d)$	0.985(0.985)	0.984(0.984)
$\eta_1(4f)$	1.076(1.077)	1.073(1.073)
$\eta_2(4f)$	0.994(0.995)	0.995(0.995)
$(1s_{1/2}   r   2p_{1/2})$	8.28	8.33
$(1s_{1/2}   r   2p_{3/2})$	8.57	8.61
$(2p_{1/2}   r   3d_{3/2})$	13.88	14.07
$(2p_{3/2}   r   3d_{3/2})$	14.30	14.51
$(2p_{3/2}   r   3d_{5/2})$	14.55	14.75
$(3d_{3/2}   r   4f_{5/2})$	26.87	27.51
$(3d_{5/2}   r   4f_{5/2})$	27.67	28.30
$(3d_{5/2}   r   4f_{7/2})$	27.97	28.60

levels,  $4d$ ,  $5d$ , etc., can feed the  $2p$  level. For these reasons several fits were made in which the amplitudes, but not the positions of the  $K$ ,  $L$ , and  $M$  lines, were allowed to vary independently to see how far from the predictions of the formalism the fitted amplitudes would be. The departure in the amplitudes averaged about 10%.

But a real discrepancy occurs in the fit to the  $M$  lines. Here, among three main peaks, that lying lowest in energy has an intensity which is 30% larger than that calculated. Only 20 keV separates this peak from the middle member of the triplet, so that change in the detection efficiency cannot account for the differ-

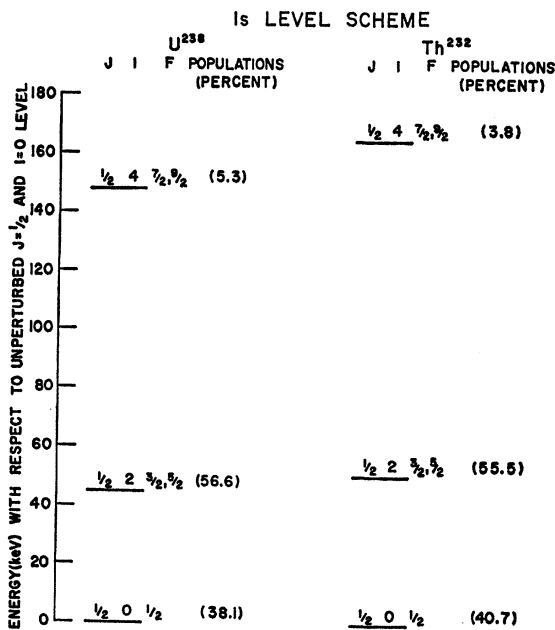


FIG. 7. Muonic  $1s$ -level scheme for  $U^{238}$  and  $Th^{232}$ . The energy levels shown are the total energies of the muon with respect to the  $1s_{1/2}$  muon state and the nucleus with respect to the  $I=0$  ground state. The muon, nuclear, and total angular momentum numbers of each state are represented by  $j$ ,  $I$ , and  $F$ , respectively. The populations of each level were calculated using the best fit to the data. Note that there is a larger than 50% probability that the nucleus will be left in an excited state by the time the muon reaches the  $1s$  level.

ence. Nor can the discrepancy be due to a departure from statistical population of the  $4f$  level, since both this peak and the larger middle peak came from the same  $4f(F=7/2)$  initial level.

We have no uniquely satisfactory explanation of this discrepancy. It can be removed by manipulating certain energy parameters. For example, a good fit can be obtained by taking the  $4f$  fine-structure splitting,  $\Delta f$ , 3 keV higher than that calculated for a point-nucleus model. However, the value of  $\Delta f$  must be close to the point-nucleus value because of the very small overlap of the  $4f$  wave functions with the nucleus. In the results presented here the value of  $\Delta f$  was fixed at the point-nucleus value.

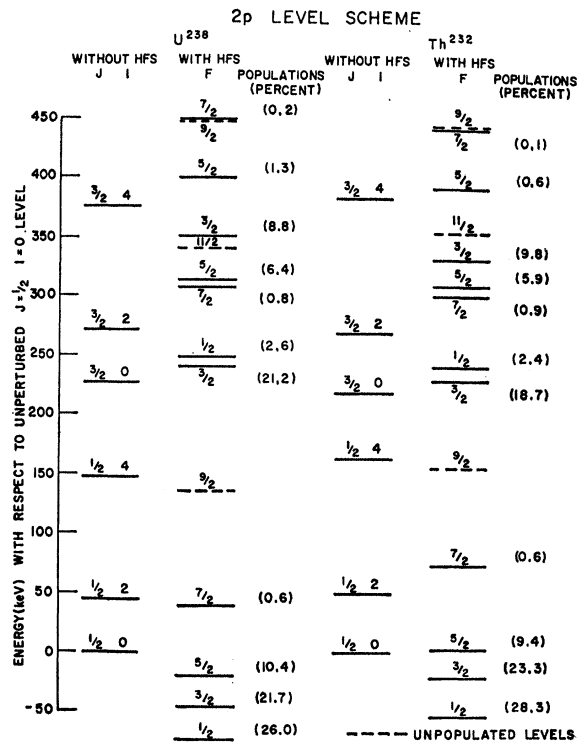


FIG. 8. Muonic  $2p$ -level scheme for  $U^{238}$  and  $Th^{232}$ . Both the unperturbed and perturbed level schemes are shown for comparison. The populations are calculated from the best fit.

The intensity discrepancy could also be removed by lowering the first nuclear rotational energy level by 2 keV in  $U^{238}$  and 3 keV in  $Th^{232}$ . But this seems unduly large if it is supposed to be due to an isomer shift in the  $M$  lines. It seems unlikely that the direct measure-

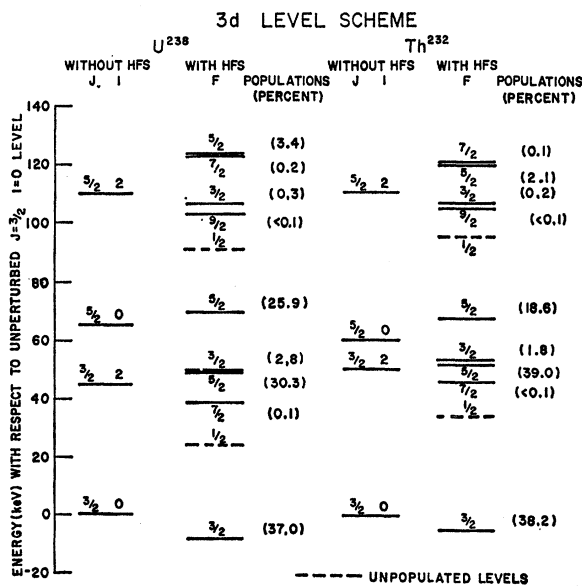


FIG. 9. Muonic  $3d$ -level scheme for  $U^{238}$  and  $Th^{232}$ .

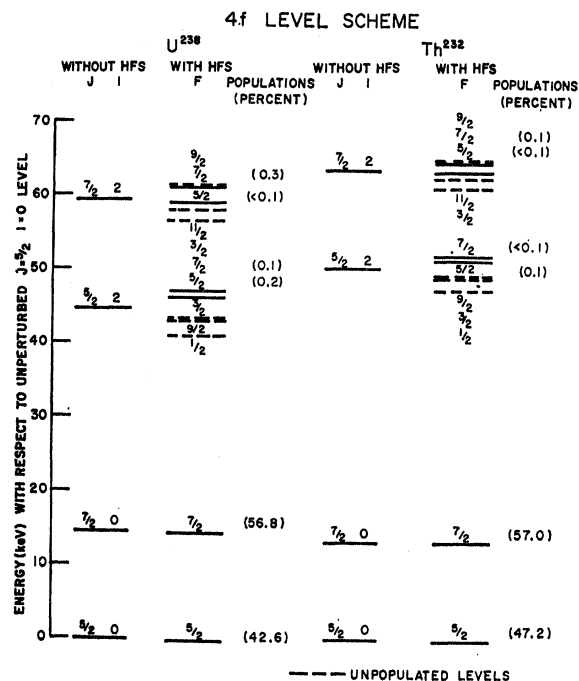


FIG. 10. Muonic 4f-level scheme for U<sup>238</sup> and Th<sup>232</sup>. The calculated populations are statistical.

ments of the nuclear rotational energies could be off by this amount.

Finally, the intensity discrepancy could be removed by lowering  $\eta_1(3d)$  and  $\eta_2(3d)$  by about 10–15%. This has the consequence that the quadrupole energies  $E(3d_{3/2}, 3d_{3/2}) = E(3d_{3/2}, 3d_{5/2})$ , while a calculation using a reasonable charge distribution would have the first energy appreciably larger than the second. On the other hand, the fact that  $\eta_1(3d)$  and  $\eta_2(3d)$  can be adjusted to bring the intensities into agreement suggests that an adjustment of the dynamic quadrupole coefficients  $\epsilon_{02}$  and  $\epsilon_{22}$  could have the same effect. This would imply a departure from the rigid-rotator model. No attempt was made here to explore the consequences of this further. However, when the first rotational-level energy was allowed to vary in  $K$ - and  $L$ -line fits, the result was a decrease in energy by 1–2 keV, without much change in the goodness of the fit.

The results from the fitting of the  $K$ ,  $L$ , and  $M$  lines are summarized in Table III. In making the  $L$ -line fits, the  $2p$  fs splitting and  $2p$  hfs splitting were fixed to those values found in the  $K$ -line fits. In the  $M$ -line fits, the  $4f$  fine structure and hfs were fixed. The  $3d$  fine-structure and hfs energy parameters determined from both the  $L$ - and  $M$ -line fits were averaged. The errors presented in Table III are three times the standard deviations (they also include the much smaller errors from the energy calibration). The tripling of the standard deviations was done because of the theoretical uncertainties in the hfs formalism such as the ignoring of the nuclear-level isomer shift, the simplifications

made in the intensity calculations, the assumption of the rigid-rotator model, and the fixing of the ratios of quadrupole energies whose values depend upon a specific charge distribution.

## VII. NUCLEAR SIZE AND SHAPE PARAMETERS

The muonic x-ray spectra of U<sup>238</sup> and Th<sup>232</sup> are reasonably well described by the hfs formalism of Sec. III without reference to any specific charge distribution except weakly through the  $\eta(nl)$  parameters and the transition matrix elements  $(nlj | r | n'l'j')$ . In this section we relate the experimental energies, presented in Table III, to a specific charge distribution.

In the analysis of recent data on spherical nuclei<sup>15,32,33</sup> the two-parameter Fermi-type charge distribution was used. We write it here in the form

$$\rho(r_N) = \rho_0 \{1 + \exp[n(r_N/R - 1)]\}^{-1}, \quad (37)$$

where  $R=c$ , the half-density radius. The skin thickness  $t$ , the radial distance between the 90 and 10% densities, is related to the skin-thickness parameter  $n$  and the half-density radius by

$$t = [(4 \ln 3)/n]R. \quad (38)$$

For  $n = \infty$ , the charge distribution is uniform up to radius  $R$  and zero beyond.

For the deformed nuclei we keep the basic Fermi model described by Eq. (37) and introduce a third parameter. There are many ways of doing this. We have chosen a model such that the shells of constant density are concentric ellipsoids of revolution with the same eccentricity. By letting  $b$  be the half-density radius of the ellipsoid's semiaxis along the axis of revolution and  $a$  the half-density radius of the ellipsoid's other semiaxis, the half-density ellipsoid is described by

$$R = a \{1 - [(b^2 - a^2)/b^2] \cos^2 \theta_N\}^{-1/2}, \quad (39)$$

with  $\theta_N$  the polar angle. Since the constant-density ellipsoids have the same eccentricity,  $n$  is a fixed parameter, and  $n$ ,  $a$ , and  $b$  constitute the three parameters. Note, too, that the skin thickness  $t$ , by Eq. (38), is not constant around the nucleus for our model. For a discussion of other three-parameter charge distributions, see De Wit *et al.*,<sup>14</sup> Acker,<sup>34</sup> and Acker and Marshall.<sup>35</sup>

It is more convenient to use two other nuclear parameters related to  $a$  and  $b$  instead of  $a$  and  $b$  themselves. One of these is the intrinsic quadrupole moment  $Q_0$  of the charge distribution. The second parameter is

<sup>32</sup> H. L. Anderson, R. J. McKee, C. K. Hargrove, and E. P. Hincks, *Phys. Rev. Letters* **16**, 434 (1966).

<sup>33</sup> H. L. Acker, G. Backenstoss, C. Daum, J. C. Sens, and S. A. De Wit, *Nucl. Phys.* **87**, 1 (1966).

<sup>34</sup> H. L. Acker, *Nucl. Phys.* **87**, 153 (1966).

<sup>35</sup> H. L. Acker and H. Marschall, *Phys. Letters* **19**, 127 (1965).

TABLE III. Unperturbed absolute energies, unperturbed fine-structure splittings, and quadrupole energies obtained by the  $\chi^2$  fits to the  $K$ ,  $L$ , and  $M$  lines of  $U^{238}$  and  $Th^{232}$ . The  $4f$  fine-structure and quadrupole energies were held constant at these values in the  $M$ -line fits. The numbers in parentheses are the theoretical energies calculated from the ellipsoidal Fermi charge distribution.

Energy (keV)	$U^{238}$	$Th^{232}$
$2p_{1/2} \rightarrow 1s_{1/2}$	$6212.5 \pm 2.5 (6212.3)$	$6124.5 \pm 2.3 (6124.3)$
$3d_{3/2} \rightarrow 2p_{1/2}$	$3182.4 \mp 0.7 (3182.5)$	$3074.3 \mp 0.7 (3074.4)$
$4f_{5/2} \rightarrow 3d_{3/2}$	$1235.4 \pm 0.6 (1234.8)$	$1180.6 \pm 0.6 (1179.7)$
$2p$ fine structure	$226.5 \mp 4.1 (228.8)$	$217.8 \mp 3.9 (219.9)$
$3d$ fine structure	$65.9 \pm 1.9 (66.0)$	$60.2 \pm 1.8 (60.9)$
$4f$ fine structure	14.7	13.4
$2p$ quad. energy	$95.5 \pm 0.9 (95.0)$	$81.3 \pm 1.1 (80.7)$
$3d$ quad. energy	$17.5 \pm 0.7 (18.8)$	$13.9 \pm 0.7 (15.2)$
$4f$ quad. energy	3.0	2.4

the equivalent radius defined by

$$R_{\text{eq}} = \left[ \frac{5}{3} \left( \int r_N^2 \rho(r_N) d^3r_N \right) / \int \rho(r_N) d^3r_N \right]^{1/2}. \quad (40)$$

$R_{\text{eq}}$  is the radius of the equivalent uniformly charged spherical nucleus. That is, if  $n = \infty$  and  $a = b$ , then  $R_{\text{eq}} = a$ . The quantity  $R_{\text{eq}}$  is a convenient parameter since, to first order, the muonic energy levels found by solving the Dirac equation are more sensitive to  $R_{\text{eq}}$  than to the other parameters. In what follows,  $r_0 = R_{\text{eq}}/A^{1/3}$  is used instead of  $R_{\text{eq}}$ . Fairly simple relationships connecting  $Q_0$  and  $r_0$  to  $a$  and  $b$  can be found. From the functional form of the Fermi distribution,

$$\begin{aligned} r_0 &= f_1(n) \left[ \frac{1}{3} (b^2 + 2a^2) \right]^{1/2} / A^{1/3}, \\ Q_0 &= \frac{2}{3} Z f_2(n) (b^2 - a^2), \end{aligned} \quad (41)$$

where  $f_1(\infty) = f_2(\infty) = 1$ . The functional forms of  $f_1(n)$  and  $f_2(n)$  are found by numerical integration of Eqs. (40) and (19).

For both  $U^{238}$  and  $Th^{232}$  a set of three parameters,  $n$ ,  $r_0$ , and  $Q_0$ , was found which best fit the energies given in Table III, excluding the  $4f$  fine-structure and quadrupole energies to which they are insensitive. The procedure for doing this was as follows.

A three-dimensional rectangular mesh was chosen in which each point in the mesh represented a set of the three parameters,  $n$ ,  $r_0$ , and  $Q_0$ . At each mesh point the seven energies corresponding to the experimental ones of Table III, excluding the two mentioned above, were calculated by means of the numerical integration of the Dirac equation. The corrections discussed in Sec. II were also included. The quadrupole energies were calculated by Eq. (27). Using a three-dimensional Lagrangian interpolation, a least-squares fit was done to the seven energies by varying the set of three parameters throughout the range of the three-dimensional mesh until the best fit was reached. The mesh was chosen fine enough so that no significant interpolation

error resulted. The approximate location of the mesh was dictated by an earlier result in which a much coarser mesh was used.

The results of the parameter fits are shown in Table IV. In Table V are shown the various calculated radiative corrections (including the small quadrupole vacuum polarization correction) made to the unperturbed muonic levels of both nuclei. These were calculated using the set of parameters in Table IV.

### VIII. COMPARISON WITH OTHER $\mu$ -ATOMIC X-RAY RESULTS

What one measures in the quadrupole hfs of muonic atoms is not  $Q_0$  by itself, but the product of the quadrupole moment and the quadrupole distribution  $Q_0 f(r)$ . Its matrix elements define the quadrupole energy (except for a constant factor) and were found by fitting the spectra as discussed earlier without reference to any specific charge distribution. Wu<sup>36</sup> has suggested that one could constrain  $Q_0$  to the "proper" value found in model-independent methods, such as in Coulomb excitation experiments, and this constraint could lead to knowledge of the distribution through  $f(r)$ . On the other hand, since the  $3d$  state samples the charge distribution in a different fashion than the  $2p$  state, the additional information of the  $3d$  quadrupole energy can, in principle, help to determine  $Q_0$  and  $f(r)$  separately. Since we have measured the  $3d$  quadrupole

<sup>36</sup> D. Hitlin, S. Bernow, S. Devons, I. Duerdoth, J. W. Kast, E. R. Macagno, J. Rainwater, K. Runge, C. S. Wu, and R. C. Barrett, in *Proceedings of the International Conference on Electromagnetic Sizes of Nuclei, Ottawa, 1967*, edited by D. J. Brown, M. K. Sundareson, and R. D. Barton (Carleton University Department of Physics, Ottawa, 1967), p. 254; K. Runge, T. T. Bardin, R. Barrett, S. Devons, D. Hitlin, E. R. Macagno, C. Nissim-Sabat, J. Rainwater, and C. S. Wu, in *Proceedings of the Williamsburg Conference on Intermediate Energy Physics, 1966*, edited by D. J. Brown, M. K. Sundareson, and R. D. Barton (Carleton University Department of Physics, Ottawa, 1967), p. 135; C. S. Wu, in *Proceedings of the International Conference on Nuclear Physics, Gallinburg, Tenn., 1966*, edited by R. L. Becker (Academic Press Inc., New York, 1967), p. 409.

TABLE IV. Results of the least-squares fit to the seven energies of Table III, using the three parameter ellipsoid Fermi charge distribution.  $t_a$  and  $t_b$  are the 90-10% skin thickness along the  $a$  and  $b$  semiaxes, respectively.  $\rho_N$  is the central nucleon density in nucleons per cubic fermi. The  $\chi^2$  is the chi squared per degree of freedom with four degrees of freedom.

Quantity	U <sup>238</sup>	Th <sup>232</sup>
$n$	14.9±0.6	14.9±0.7
$r_0$ (F)	1.2186±0.0007	1.2160±0.0008
$Q_0$ (b)	11.47±0.13	9.83±0.16
$a$ (F)	6.501±0.024	6.506±0.28
$b$ (F)	8.396±0.033	8.189±0.038
$t_a$ (F)	1.92±0.07	1.92±0.08
$t_b$ (F)	2.48±0.09	2.42±0.10
$\rho_N$ (F <sup>-3</sup> )	0.153±0.002	0.153±0.003
$\chi^2$	1.27	1.57

energy, we have chosen the latter course. But, although we have obtained good fits to our elliptical model, our result for  $Q_0$  and  $f(r)$  still depends on the choice of the Fermi shape.

Therefore, direct comparisons of our nuclear parameters with the results of other investigators<sup>14,26,36,37</sup> is not possible because of the different nuclear models used, although most use the Fermi shape. The Columbia group<sup>36</sup> uses a four-parameter model in which the half-density radius and skin thickness have a different angular dependence. In their fits to the isotopes of tungsten, they find a preference for a constant skin thickness, although the resulting  $Q_0$  disagrees with Coulomb excitation results. The Carnegie<sup>37</sup> and CERN<sup>14</sup> groups use a model similar to ours, that is, a model deformed all the way to the core. Pieper and Greiner<sup>26</sup> have used a dynamic rotational vibration model described by two parameters in which the skin thickness is generated by the rotation vibration fluctuations of the surface. They have shown that this model fits the CERN<sup>14</sup> data for U<sup>238</sup>.

A reasonable comparison can be made with the results of De Wit *et al.*,<sup>14</sup> who have also used a three-parameter Fermi distribution whose shells of constant density are concentric and have equal eccentricity also, but are described by a spheroidal function somewhat different from the ellipsoid of revolution. Their model (following them, we shall call it the deformed model to distinguish from our model, the ellipsoid model) is written

$$\rho(r_N) = \rho_0 [1 + \exp\{(4 \ln 3)[r_N(1 - \beta Y_{20}(\theta_N)) - c]/t\}]^{-1}. \quad (42)$$

The dimensionless quantity  $\beta$  describes the deformation. The parameters  $c$  and  $t$  are a type of average half-density radius and skin thickness.

In order to make any kind of comparison between the two models it is necessary to find the three parameters of the deformed model,  $\beta$ ,  $c$ , and  $t$ , in terms of the three parameters of the ellipsoid model,  $a$ ,  $b$ , and  $n$ . Since the functional forms of the two models are not identical, there is no unique way of defining  $\beta$ ,  $c$ , and  $t$  in terms of  $a$ ,  $b$ , and  $n$ .

However, if the following definitions are made:

$$\beta = \left[ \frac{1}{6} \left( \frac{16\pi}{5} \right)^{1/2} \frac{b^2 - a^2}{b^2} \right] \left( 1 - \frac{1}{3} \frac{b^2 - a^2}{b^2} \right)^{-1},$$

$$c = a \left\{ 1 - \frac{1}{3} [(b^2 - a^2)/b^2] \right\}^{-1/2}, \quad (43)$$

$$t = [(4 \ln 3)/n]c,$$

then the ellipsoid model can be rewritten as

$$\rho(r_N) = \rho_0 [1 + \exp\{(4 \ln 3)[r_N(1 - 2\beta Y_{20}(\theta_N))^{1/2} - c]/t\}]^{-1}. \quad (44)$$

TABLE V. Radiative corrections calculated for the unperturbed energy levels of U<sup>238</sup> and Th<sup>232</sup>. Energies are in keV.

Unperturbed level of U <sup>238</sup>	Vacuum polarization	Lamb shift	Anomalous magnetic moment
1s <sub>1/2</sub>	74.6	-2.3	-0.48
2p <sub>1/2</sub>	39.9	-0.8	0.28
2p <sub>3/2</sub>	37.0	-0.6	-0.27
3d <sub>3/2</sub>	14.3	-0.04	0.10
3d <sub>5/2</sub>	13.3	-0.02	-0.06
4f <sub>5/2</sub>	5.3	<-0.001	0.02
4f <sub>7/2</sub>	5.1	<-0.001	0.01
Unperturbed level of Th <sup>232</sup>	Vacuum polarization	Lamb shift	Anomalous magnetic moment
1s <sub>1/2</sub>	73.0	-2.3	-0.47
2p <sub>1/2</sub>	38.4	-0.7	0.27
2p <sub>3/2</sub>	35.6	-0.6	-0.25
3d <sub>3/2</sub>	13.5	-0.04	0.09
3d <sub>5/2</sub>	12.6	-0.02	-0.06
4f <sub>5/2</sub>	5.0	<-0.001	0.02
4f <sub>7/2</sub>	4.8	<-0.001	-0.01
Vacuum polarization correction to quadrupole energy	U <sup>238</sup>	Th <sup>232</sup>	
$E(2p_{1/2}, 2p_{3/2})$	0.34	0.29	
$E(3d_{3/2}, 3d_{5/2})$	0.04	0.03	

<sup>37</sup> R. E. Cote, W. V. Prestwich, A. K. Gaigalas, S. Raboy, C. C. Trail, R. A. Carrigan, Jr., P. D. Gupta, R. B. Sutton, and M. N. Suzuki, in *Proceedings of the International Conference on Electromagnetic Sizes of Nuclei, Ottawa, 1967* (the College of William and Mary, Williamsburg, 1966), p. 35.

TABLE VI. Comparison between the CERN work and the present work. All energies are given in keV. Columns 3 and 5 are the differences between the present work and the CERN work. The parameters  $c$ ,  $t$ , and  $\beta$  found by De Wit *et al.*<sup>a</sup> describe the deformed model Eq. (42). These same parameters, found in the present work, have been calculated by Eq. (43) using the ellipsoid model parameters of Table IV.

Quantity	$U^{238}$		$Th^{232}$	
	De Wit <i>et al.</i>	Difference	De Wit <i>et al.</i>	Difference
$2p_{1/2} \rightarrow 1s_{1/2}$	6213.6	-1.1	6125.0	-0.5
$3d_{3/2} \rightarrow 2p_{1/2}$	3186.7	-4.3	3077.4	-3.1
$4f_{5/2} \rightarrow 3d_{3/2}$	1233.8	1.6	1178.6	2.0
$2p$ fine structure	228.8	-2.3	219.9	-2.1
$3d$ fine structure	65.9	0.0	60.7	-0.5
$4f$ fine structure	14.6	0.1	13.4	0.0
$E(2p_{1/2}, 2p_{3/2})$	94.7	0.8	81.6	-0.3
$E(2p_{3/2}, 2p_{5/2})$	95.8	0.8	82.3	-0.3
$E(3d_{3/2}, 3d_{5/2})$	21.1	-1.1	17.3	-1.5
$E(3d_{5/2}, 3d_{7/2})$	18.5	-1.0	15.2	-1.3
$E(3d_{7/2}, 3d_{9/2})$	18.2	-1.0	14.9	-1.2
$c$ (F)	$7.15 \pm 0.03$	-0.17	$7.10 \pm 0.04$	-0.15
$t$ (F)	$1.46 \mp 0.12$	0.60	$1.49 \mp 0.14$	0.56
$\beta$	$0.253 \pm 0.003$	-0.009	$0.23 \pm 0.01$	-0.008
$Q_0$ (b)	$11.25 \pm 0.15$	0.22	$9.8 \pm 0.3$	0.03
$\rho_N$ ( $F^{-3}$ )	$0.147 \pm 0.003$	0.006	$0.147 \pm 0.003$	0.006

<sup>a</sup> Reference 14.

For small  $\beta$ , the two models become identical, since  $(1 - 2\beta Y_{20})^{1/2} = 1 - \beta Y_{20} + O(\beta^2)$ .

The comparison is shown in Table VI. The agreement in the quadrupole moments is excellent. Note, however, that De Wit *et al.* find a larger  $c$  and considerably smaller  $t$  than the present results. Part of this may be due to the slight difference in the two models. Part of it may also be due to the inclusion of three additional, although rather small, radiative corrections in the present work: the Lamb shift, anomalous magnetic moment, and the quadrupole vacuum polarization.

## IX. QUADRUPOLE MOMENT

In addition to muonic x rays, there are several other experimental techniques that have been used to measure the nuclear electric quadrupole moment. These techniques include spectroscopic measurements, Coulomb excitation, and giant dipole resonances. Since these other techniques are model-independent, a direct comparison with the results of muonic x rays is not possible. The value of  $Q_0$  that is determined in the present work is really a parameter of a specific charge distribution and can be quite different for different charge distributions. Nevertheless, it is instructive to make the comparison, since an agreement of  $Q_0$  determined by muonic x-ray experiments with the "proper" value of  $Q_0$  determined by the model-independent methods would show that the chosen charge distribution is reasonably correct (Fig. 11).

The spectroscopic hfs is described by a theory which is essentially identical with the  $\mu$ -atomic hfs theory presented in this paper; but the electric quadrupole interaction between the nucleus and the electrons found in the atom, while formally the same, leads to quite different results due to the large number of electrons in the atom and the smaller electronic mass. In the first place, the orbit of the electron, even for the innermost  $K$  shell, is much larger than the size of the nucleus. Thus, except for a small finite nuclear size correction,

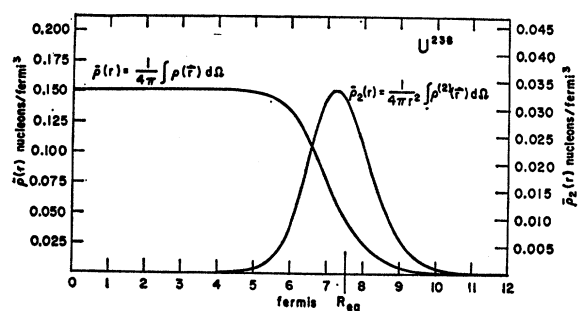


FIG. 11. Monopole and angular-averaged dipole charge distributions calculated for  $U^{238}$  using the ellipsoid Fermi model defined by Eqs. (37) and (39). The nuclear shape parameters used were the ones that best fit the data as shown in Table IV.

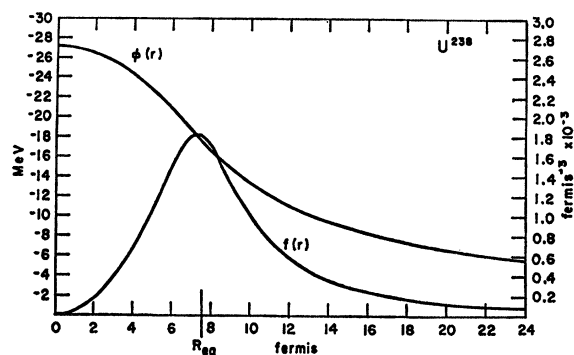


FIG. 12. Monopole potential energy and penetration factor calculated for  $U^{238}$  using the charge distribution shown in Fig. 11.

the electronic hyperfine interaction is independent of the detailed shape of the nucleus. This is in sharp contrast to the muonic case.

In addition, the electronic wave functions needed to relate the spectroscopic measurement to the quadrupole moment are not as well known due to the many-electron character in the atom. This difficulty is not present in the muonic case where only the uncertainty in the nuclear size and shape makes the muonic wave functions uncertain (Figs. 12 and 13).

Finally, for both spectroscopic and muonic cases, no static hfs occurs for nuclei of ground-state spins 0 or  $\frac{1}{2}$ . For the muonic case, a dynamic hfs can occur that involves the excited states of the nucleus. For the spectroscopic case, no dynamic hfs occurs, because the quadrupole interaction energy is orders of magnitude less than the first nuclear excited state. Thus, no spectroscopic data exist for  $U^{238}$  and  $Th^{232}$ .

In Coulomb excitation experiments, one bombards the nucleus with low-energy protons or heavier ions, such as  $\alpha$  particles, and studies the inelastic scattering events in which the nucleus is excited to one of the rotational levels. One measures from such experiments the electric quadrupole reduced transition probability  $B(E2, I_i \rightarrow I_f)$  between the initial state of spin  $I_i$  and final state of spin  $I_f$ . If the rigid-rotator model with the symmetry axis is assumed, the transition probability is related to the quadrupole moment by

$$B(E2, I_i \rightarrow I_f) = (5/16\pi) e^2 Q_0^2 C(I_i 2 I_f; K 0 K)^2. \quad (45)$$

This result is model-dependent in so far as it depends on the Bohr-Mottelson model, but it is independent of the choice of the cylindrically symmetric charge distribution. Note, too, that the Coulomb excitation experiments do not determine the sign of the quadrupole moment.

There are several independent ways of finding the reduced transition probability in a Coulomb excitation experiment. One way is to measure the inelastic cross section which is proportional to  $B(E2, I_i \rightarrow I_f)$  with  $I_i$

the ground state and  $I_f$  the excited state. The other methods study the decay of the excited nucleus back to the ground state (or some other intermediate state). In this second group of methods, one way is to measure the lifetime of the excited state which is proportional to  $B(E2, I_i \rightarrow I_f)$  with  $I_i$  the excited state the  $I_f$  the ground state (or intermediate state). Another is to measure the yield of conversion electrons and the third way is to measure the yield of the deexcitation  $\gamma$  rays.

In order to relate the reduced transition probability to the experimentally observed quantities in the second group of methods, the conversion coefficient of the conversion electrons must be used. It is the common practice to use the theoretically derived conversion coefficients. These depend upon a knowledge of the electronic wave functions which are uncertain to some extent. Thus, the transition probability, and hence the quadrupole moment, measured by one of the methods in the second group has an uncertainty due to the conversion coefficient. For a detailed discussion of Coulomb excitation, including the theory and experimental difficulties, see the review paper by Alder *et al.*<sup>38</sup>

In giant dipole resonance experiments using a highly deformed nucleus, two closely spaced resonances occur corresponding to the major and minor axes of the deformed nucleus. The spacing of the two resonances is proportional to the quadrupole moment. However, since the resonances take place at high energies (on the order of 10 MeV), the dynamic quadrupole moment associated with highly excited nuclear states is the quantity that is really measured. Since the nucleus probably does not have the same shape in a very high excited state, only qualitative agreement between the quadrupole measurements in muonic atoms and giant dipole resonances can be expected.

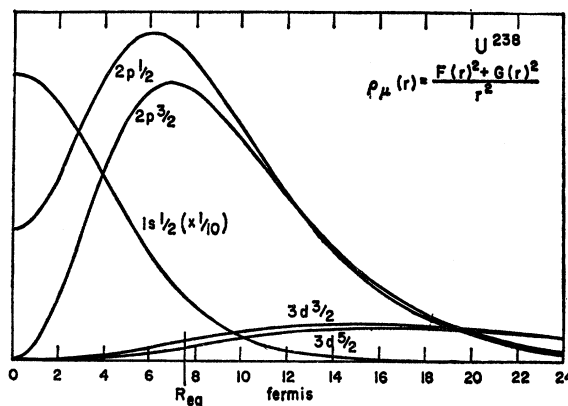


FIG. 13. Unperturbed muon  $1s$ ,  $2p$ , and  $3d$  wave functions calculated for  $U^{238}$  by solving numerically the Dirac equation (9). The monopole potential energy used is shown in Fig. 12.

<sup>38</sup> K. Alder, A. Bohr, T. Huus, B. Mottelson, and A. Winther, *Rev. Mod. Phys.* **28**, 432 (1956).

TABLE VII. Comparison of the quadrupole moment  $Q_0$  and deformation parameter  $\beta$  with other methods. Quadrupole moment is in b. Reference a uses  $Q_0 = 3(5\pi)^{-1/2}ZR_0^2\beta(1+0.16\beta)$  with  $R_0 = 1.2A^{1/3}$  F to define  $\beta$ ; Ref. b uses  $Q_0 = \frac{2}{3}ZR_0^2\beta(1+0.50\beta)$  with  $R_0 = 1.2A^{1/3}$  F to define  $\beta$ . Reference 14 and the present work define  $\beta$  in Sec. VIII.

	$U^{238}$		$Th^{232}$	
	$Q_0$	$\beta$	$Q_0$	$\beta$
Coulomb excitation: half-life <sup>a</sup>	10.52±0.48	0.268	9.25±0.23	0.243
Coulomb excitation: cross section <sup>a</sup>	11.25±0.25		9.87±0.25	
Coulomb excitation: conversion electrons <sup>b</sup>	11.5±0.9	0.251	10.8±0.8	0.245
Coulomb excitation: deexcitation $\gamma$ <sup>c</sup>			8.0±0.6	
Muonic x rays <sup>d</sup>	11.25±0.15	0.253±0.003	9.8±0.3	0.23±0.01
Present work	11.47±0.13	0.244±0.002	9.83±0.16	0.222±0.003

<sup>a</sup> R. E. Bell, S. Bjornholm, and J. C. Severiens, Kgl. Danske Videnskab. Selskab, Mat.-Fys. Medd. **32**, 12 (1960).

<sup>b</sup> D. H. Rester, M. S. Moore, F. E. Durham, and C. M. Class, Nucl.

Phys. **22**, 104 (1961).

<sup>c</sup> F. K. McGowan and P. H. Stelson, Phys. Rev. **120**, 1803 (1960).

<sup>d</sup> Reference 14.

Along with the quadrupole moment, quite frequently the deformation parameter is shown in the literature. Usually,  $\beta$  is defined proportional to the difference between the major and minor axes. But to relate  $\beta$  to  $Q_0$  a specific charge distribution is needed. For the three-parameter Fermi-type charge distribution used in the present work,  $\beta$  is defined in Eq. (43) and related to  $Q_0$  by Eq. (41). For the three-parameter charge distribution used by De Wit *et al.*<sup>14</sup> discussed in Sec. VIII,  $\beta$  is defined in Eq. (42). For the Coulomb excitation work, it is a common practice to assume a uniform charge distribution with a spheroidal surface given by

$$R(\theta, \phi) = R_0[1 + \beta Y_{20}(\theta, \phi)], \quad (46)$$

with  $R_0 = 1.2A^{1/3}$  F. Then, to order  $\beta^2$ ,

$$Q_0 = 3(5\pi)^{-1/2}ZR_0^2\beta(1+0.36\beta). \quad (47)$$

The values of  $Q_0$  found in the present work, 11.47±0.13 and 9.83±0.16 b for  $U^{238}$  and  $Th^{232}$ , respectively, are in good accord with other measurements as shown in Table VII. Only the experimental errors on  $Q_0$  found by the half-life measurements are given; they do not include the uncertainties in the conversion coefficients.

## X. CONCLUSIONS

The principal purpose of this experiment was to determine the quadrupole moments as well as the radial and skin-thickness parameters of two highly deformed spin-zero nuclei,  $U^{238}$  and  $Th^{232}$ . To do this, we have assumed the Bohr-Mottelson axially symmetric rigid-rotator model for the dynamic quadrupole hyperfine interaction and have fitted the hfs of the  $K$ ,  $L$ , and  $M$  lines by adjusting certain energy parameters (unperturbed absolute energies, fine-structure splittings, and hfs energies) until good fits were obtained to the  $U^{238}$

and  $Th^{232}$  spectra. The anomalies that occurred in the fits—principally, the poor fit to the intensity of one of the  $M$  lines for both nuclei and the poor fit to the position of one of the upper group  $K$  lines in  $U^{238}$ —can possibly be explained by discarding the assumption of rigidity in the nucleus, but this idea was not pursued in the present work.

The energy parameters were related to a specific deformed nuclear charge distribution by a numerical solution of the Dirac equation. The assumed charge distribution was of the Fermi type whose shells of constant density are concentric ellipsoids of revolution all with the same eccentricity; thus, for this model the deformation is not merely skin deep but goes to the center of the nucleus. The CERN group<sup>14</sup> have tried fitting their data obtained from several deformed nuclei with a Fermi-type “hard-core” model, a charge distribution in which the deformation is concentrated near the surface, but they found better results by using the “deformed model” with its deformation extending throughout the nucleus. They also point out that this preference of deformed over hard core depends on the use of the Fermi form and thus may not be necessarily extended to other types of charge distributions. In any case, for a thin skin in the Fermi model, all the inner shells of constant density have almost the same density, so that the inner regions of both types of models are “hard-core.” Figures 11–13 shows this for the ellipsoid model. In the present work, we have made no attempt to fit our data with the hard-core model; we get reasonably good fits with our own deformed model.

The value of the deformation parameter of  $\beta$  for the present work, 0.244±0.002 and 0.222±0.003 for  $U^{238}$  and  $Th^{232}$ , respectively, shows how large the deformations are in these nuclei. On the other hand, the central density, 0.153±0.002 and 0.153±0.003 nucleons per

cubic fermi, respectively, is only slightly below the value of 0.158 nucleons per cubic fermi which characterizes most spherical nuclei.<sup>15,36</sup> Thus, nuclear matter elongates but does not change in central density as it departs from the closed-shell structure.

The intrinsic quadrupole moments were found to be  $(11.47 \pm 0.13) \times 10^{-24}$  cm<sup>2</sup> for U<sup>238</sup> and  $(9.83 \pm 0.16) \times 10^{-24}$  cm<sup>2</sup> for Th<sup>232</sup> and agree very well with the results of De Wit *et al.*<sup>14</sup> as shown in Table VI.

#### ACKNOWLEDGMENTS

I would like to thank Professor H. L. Anderson for suggesting this problem and for his generous assistance and encouragement in the preparation, execution, and interpretation of this experiment. I would also like to

thank my collaborators Richard D. Barton, Clifford K. Hargrove, E. P. Hincks, James D. McAndrew, Madhu S. Dixit, Harlan J. Evans, and Dan Kessler for their effort and support during the course of the experiment. I am indebted to I. L. Fowler and H. L. Malm of the Chalk River Nuclear Laboratories of Atomic Energy of Canada Ltd. for the fabrication of the Ge(Li) detector and for helping to mount it. I am grateful for the technical assistance rendered by Rudy Gabriel, J. P. Legault, John Lillberg, William Miles, Paul Plowe, and John Redfern. I would also like to thank Frank Castorf and Mrs. Serena Torres for their computer programming assistance. And, finally, I thank Mrs. Ann Scott for her patience in typing the many drafts of this paper.

### Studies of Os<sup>189</sup>: Gamma Rays, Lifetimes, and Mössbauer Effect\*

M. C. GREGORY,<sup>†</sup> B. L. ROBINSON, AND S. JHA  
Case Western Reserve University, Cleveland, Ohio 44106  
(Received 21 October 1968)

The  $\gamma$ -ray energies and intensities in the decay of iridium-189 have been measured with Ge(Li) and Si(Li) detectors, and the internal-conversion coefficients of 15 lines have been estimated. The mean life of the 276-keV state was found to be less than 0.4 nsec by electronic means. Limits were established for the mean life of the 95.3-keV state by the Mössbauer effect (greater than 0.2 nsec) and by electronic means (less than 0.4 nsec). The mean life of the 69.6-keV level was found to be  $2.35 \pm 0.06$  nsec, and a single line of corresponding width was observed in the Mössbauer effect. The nuclear Zeeman effect gave the magnetic moment of the 69.6-keV state as  $0.965 \pm 0.020 \mu_N$ , with  $E2/M1 = 0.57 \pm 0.21$  and an internal magnetic field of  $1.085 \pm 0.052$  MG acting on the osmium nucleus in a dilute iron alloy. The electromagnetic properties of the 69.6-keV level are completely consistent with its pure rotational character.

#### I. INTRODUCTION

**T**HE level structure of osmium-189 and the properties of its excited states have not been well studied. The level structure is inferred from the studies of the radioactive decay of 24-h rhenium-189<sup>1,2</sup> and 13.3-day iridium-189.<sup>1,3</sup> Although transition energies have been measured accurately by  $\beta$ -ray spectroscopy and internal-conversion ratios have been estimated, high-resolution  $\gamma$ -ray studies have not been carried out. From Coulomb excitation work<sup>4-6</sup> the  $B(E2)$  values

for the 69.6-, 95.3-, 219.4-, and 233.6-keV levels have been extracted.

The partial level scheme of osmium-189 is shown in Fig. 1. The ground state of osmium-189 is  $\frac{3}{2}^-$ , its magnetic dipole moment is  $+0.6566 \mu_N$ , and its electric quadrupole moment is  $+0.91 \pm 0.10$  b.<sup>7</sup> The 69.6-keV level ( $\frac{5}{2}^-$ ) is interpreted to be the first rotational state built on the ground state. Its mean life has not been directly measured but it is estimated to be 2.4 nsec, based upon the  $B(E2)$  value extracted from Coulomb excitation and the multipolarity mixture ratio extracted from internal-conversion data. The 36.3-keV state ( $\frac{1}{2}^-$ ) is supposed to be an intrinsic state.<sup>7a</sup> No measurement of its lifetime has been made, but the 36.3-keV transition to the ground state is an almost pure  $M1$  transition. The 95.3-keV state has been interpreted as the first rotational state built on the 36.3-keV intrinsic state. Its lifetime is inferred to be 0.86 nsec,

\* From the Ph.D. thesis of M. C. Gregory, Case Western Reserve University, 1968.

<sup>†</sup> Present address: Lawrence Radiation Laboratory, Livermore, Calif.

<sup>1</sup> A. Artna, Nucl. Data **1B**, 85 (1966).

<sup>2</sup> B. Craseman, G. T. Emery, W. R. Kane, and M. L. Perlman, Phys. Rev. **132**, 1681 (1963).

<sup>3</sup> B. Harmatz, T. H. Handley, and J. W. Mihelich, Phys. Rev. **128**, 1186 (1962).

<sup>4</sup> D. H. Rester, M. S. Moore, F. E. Durham, and C. M. Class, Nucl. Phys. **22**, 104 (1961).

<sup>5</sup> F. K. McGowan, P. H. Stelson, R. L. Robinson, and J. L. C. Ford, Oak Ridge National Laboratory Report No. ORNL-3425, 1963, p. 26 (unpublished).

<sup>6</sup> A. Z. Hryniewicz, B. Sawicka, J. Styczen, S. Szymczyk, and M. Szawlowski, Acta Phys. Polon. **31**, 437 (1967).

<sup>7</sup> G. Himmel, Z. Physik **211**, 68 (1968).

<sup>7a</sup> Note added in the proof. P. Kienle *et al.* have studied the Mössbauer effect with the 36.3-keV  $\gamma$  ray. The mean life and the magnetic moment of the 36.3-keV state are  $(0.72 \pm 0.04)$  nsec and  $(0.226 \pm 0.029) \mu_N$ , respectively (private communication).